Applied Mathematical Modelling 159 (2026) 117044

Contents lists available at ScienceDirect

Applied Mathematical Modelling

journal homepage: www.elsevier.com/locate/apm

Elastomagnetic amplifier friction dampers: Analytical modelling and closed-form optimal design for superior vibration mitigation

Sudip Chowdhury *, Sondipon Adhikari

Infrastructure and Environment, James Watt School of Engineering, The University of Glasgow, Glasgow, Scotland, United Kingdom

ARTICLE INFO

Keywords:
Elastomagnetic amplifier
Elastomagnetic amplifier friction damper
H_2 and H_∞ optimisations
Frictional damping element
Magnetic stiffness

ABSTRACT

The performance of conventional tuned mass dampers (TMDs) is limited by narrow tuning bandwidths, high sensitivity to parameter variations, and the requirement for substantial auxiliary mass and large relative displacements to achieve effective vibration reduction. Advanced configurations, including inerter and inertial amplifier systems, improve effective inertia. However, they lack the ability to simultaneously modulate stiffness and damping, which limits their performance under broadband and varying dynamic excitations. This paper addresses the need for a vibration mitigation device that can overcome these limitations. An elastomagnetic amplifier is introduced as a novel mechanism that enables simultaneous enhancement of effective mass and controllable stiffness. This concept is further extended by integrating a frictional damping element to develop a nonlinear elastomagnetic amplifier friction damper (EAFD). The governing equations of motion are derived using the energy method and the Euler-Lagrange equation. Closed-form expressions for the optimal design parameters are obtained using H_2 and H_∞ optimisation techniques. Frequency-domain responses are analysed using transfer function formulations and validated through numerical simulations employing the Newmark-beta method. The EAFD achieves a 23.99% improvement in vibration reduction compared to conventional TMDs. The results demonstrate robust and efficient performance under harmonic, random, and seismic excitations.

1. Introduction

Modern engineering systems demand effective vibration mitigation across a wide range of applications, including mechanical systems, precision equipment, and civil structures [1–3]. In such systems, vibration control performance is governed by key physical parameters such as mass, stiffness, damping, and excitation characteristics [4–6]. Tuned mass dampers (TMDs) provide a reliable passive control strategy due to their simplicity, ease of implementation, and ability to attenuate resonant responses without external energy input [7–12]. A conventional TMD consists of a secondary mass attached to the primary structure through a spring and viscous damper, tuned to oscillate out of phase with the structural motion, thereby transferring and dissipating vibrational energy. These systems have been successfully applied in high-rise buildings, long-span bridges, and precision instruments subjected to wind, seismic, and operational excitations [13–22]. To enhance energy dissipation, several variants have been developed, including tuned mass friction dampers, friction vibration absorbers, and negative stiffness systems, which improve nonlinear energy dissipation and low-frequency performance [23–31]. Despite these advantages, these systems remain sensitive to tuning accuracy and often rely on

* Corresponding author.
E-mail address: Sudip.Chowdhury@glasgow.ac.uk (S. Chowdhury).

https://doi.org/10.1016/j.apm.2026.117044
Received 19 February 2026; Received in revised form 20 April 2026; Accepted 8 May 2026
Available online 12 May 2026

Nomenclature

Symbols

m_s	Mass of the primary structure
m_d	Mass of the damper
m_a	Mass of the amplifier magnet
m_b	Effective mass of the elastomagnetic amplifier
k_s	Stiffness of the primary structure
k_d	Stiffness of the damper spring
k_a	Stiffness of the amplifier spring
k_b	Effective stiffness of the elastomagnetic amplifier
c_s	Damping coefficient of the primary structure
c_b	Damping coefficient of the damper
c_e	Equivalent linearised damping coefficient
u_s	Displacement of the primary structure
u_d	Relative displacement of the damper
y_d	Displacement of the amplifier
x_a, y_a	Horizontal and vertical displacements of amplifier mass
$(\dot{\cdot}), (\ddot{\cdot})$	First and second time derivatives
ϕ	Magnetic amplifier angle
b	Vertical spacing between fixed magnets
c	Horizontal distance between magnets
$r^{\pm}$	Distance between amplifier and fixed magnets
α	Magnetic strength coefficient
A_0, A_1, A_2, A_3	Magnetic force expansion coefficients
V_m	Magnetic potential energy
T, V	Kinetic and potential energy
L	Lagrangian of the system

Dimensionless parameters

$\mu_d = m_d/m_s$	Damper-to-structure mass ratio
$\mu_a = m_a/m_d$	Amplifier-to-damper mass ratio
$\kappa = k_a/k_d$	Amplifier stiffness ratio
$\nu = A_1/k_b$	Magnetic stiffness ratio
$\gamma_b = m_b/m_d$	Magnetic amplification factor
κ_b	Effective stiffness amplification factor

Dynamic parameters

ω_s	Natural frequency of the structure
ω_d	Natural frequency of the damper
$\Omega = \omega/\omega_s$	Frequency ratio
$\Omega_d = \omega_d/\omega_s$	Damper frequency ratio
ξ_s	Damping ratio of the structure
ξ_d	Damping ratio of the damper
q	Complex frequency variable ($q = i\omega$)

Statistical quantities

σ_{u_d}	Standard deviation of damper displacement
$\sigma_{\dot{u}_d}$	Standard deviation of damper velocity
S_0	Power spectral density of excitation

Excitation terms

u_g	Base displacement excitation
$\dot{u}_g, \ddot{u}_g$	Base velocity and acceleration
μ	Friction coefficient
g	Acceleration due to gravity

substantial auxiliary mass or large relative displacements, which limits their effectiveness under broadband and varying dynamic excitations.

The goal of TMD design advancements is to overcome these limitations through the development of enhanced tuning strategies and optimisation techniques [32–35]. Modern optimisation frameworks enable systematic parameter selection and improved robustness under varying dynamic conditions. For instance, the optimal tuning frequency and damping ratios of TMDs are commonly determined using H_2 optimisation [36,37], which minimises the mean-square dynamic response under random excitations [38,39]. Similarly, these parameters are obtained from the dynamic responses [40] of TMD-controlled structures exposed to harmonic excitations [41] using H_∞ optimisation, which focuses on reducing the worst-case response and ensuring robustness under bounded disturbances. In addition to these classical approaches, gradient-based, robust, and metaheuristic optimisation techniques such as genetic algorithms, particle swarm optimisation, and differential evolution have been widely used to address nonlinear and multi-objective design problems [42,43]. Parallel to these developments, inerter-based systems have gained attention for their ability to enhance effective inertia without increasing physical mass, while inertial amplifiers utilise geometric and kinematic configurations to amplify inertial forces and improve vibration attenuation [44–47]. In a broader context, advanced continuum and mathematical modelling frameworks, such as micromorphic theory and fractional formulations, have been developed to describe materials with microstructural characteristics, intrinsic rotations, and memory-dependent behaviour [48,49]. These approaches enable the incorporation of nonlocal effects and complex interactions that are not adequately captured by classical models [50,51]. However, these systems still exhibit several limitations. Inerter-based devices introduce mechanical complexity and sensitivity to parameter tuning, while inertial amplifier systems primarily enhance effective mass without significantly influencing stiffness. Furthermore, many optimisation approaches rely heavily on numerical procedures, which can be computationally expensive and may not provide direct analytical insight into system behaviour. These limitations highlight the need for advanced vibration mitigation strategies capable of simultaneously improving effective mass, stiffness, and damping characteristics.

To address these limitations, this paper introduces a novel vibration mitigation framework based on an elastomagnetic amplification mechanism. The elastomagnetic amplifier is proposed as a new device that enables simultaneous enhancement of effective mass and controllable stiffness through magnetic interactions, including the generation of effective negative stiffness. This capability allows significant modulation of system dynamics without increasing static mass, which is not achievable using conventional or existing amplification-based systems. The concept is further extended by integrating a frictional damping element within the amplifier framework to develop a nonlinear elastomagnetic amplifier friction damper. This unified mechanism combines mass amplification, stiffness modulation, and nonlinear energy dissipation, thereby overcoming the fundamental limitations of conventional and advanced vibration control devices. The governing equations of motion of the coupled system are derived using the energy method and the Euler-Lagrange equation. In addition, closed-form expressions for the optimal design parameters are obtained using H_2 and H_∞ optimisation techniques, providing direct analytical insight into system behaviour and enabling efficient and reliable design implementation. Finally, the developed system is systematically compared with conventional tuned mass dampers to evaluate its vibration mitigation capability and to assess its effectiveness in addressing limitations related to bandwidth, adaptability, and mass requirements.

2. Elastomagnetic amplifier

The schematic diagram of the elastomagnetic amplifier is shown in Fig. 1(a).

ϕ defines the magnetic amplifier angle. An upward movement is considered for the central mass m_d. This mass is connected by a spring with stiffness of k_d. In addition, the amplifier itself has a spring with stiffness of k_a. The amplifier magnetic mass has displacements of x_a and y_a. Accordingly, the amplifier displacements are derived as

$$y_a = \frac{y_d}{2} \quad \text{and} \quad x_a = \frac{y_d}{2\tan\phi} \tag{1}$$

where y_d denotes the displacement of the amplifier. The static horizontal distance at the reference position between the amplifier magnet and the fixed magnet wall is indicated by the parameter $c > 0$. The instantaneous horizontal separation is $c + x_a$ because the horizontal displacement x_a satisfies $x_a > 0$ when the amplifier magnet moves away from the wall and $x_a < 0$ when it moves towards the wall. On each wall, the amplifier magnet m_a is situated halfway between two fixed magnets at $\pm b/2$. Consequently, $r^{\pm}_{L,R}$ represents the instantaneous distances between the amplifier magnet and the fixed magnets on the left and right sides, where the superscripts ve + and ve - represent the lower and upper fixed magnets, respectively. Accordingly, the distances between the amplifier magnet and the lower and upper fixed magnets on the left side are derived as

$$r_L^+ = \sqrt{\left(c + \frac{y_d}{2\tan\phi}\right)^2 + \left(\frac{y_d}{2} + \frac{b}{2}\right)^2} \quad \text{and} \quad r_L^- = \sqrt{\left(c + \frac{y_d}{2\tan\phi}\right)^2 + \left(\frac{y_d}{2} - \frac{b}{2}\right)^2} \tag{2}$$

Simultaneously, the distances between the amplifier magnet and the lower and upper fixed magnets on the right side are derived as

$$r_R^+ = \sqrt{\left(c + \frac{y_d}{2\tan\phi}\right)^2 + \left(\frac{y_d}{2} + \frac{b}{2}\right)^2} \quad \text{and} \quad r_R^- = \sqrt{\left(c + \frac{y_d}{2\tan\phi}\right)^2 + \left(\frac{y_d}{2} - \frac{b}{2}\right)^2} \tag{3}$$

Because of the system's geometric symmetry and the local definition of the displacement coordinates, the amplifier magnet experiences the same magnetic interaction distances on the left and right sides for a given configuration. Eq. (1) is differentiated with respect to time. Accordingly, the velocities of the amplifier mass in x and y-directions are derived as

$$\dot{y}_a = \frac{\dot{y}_d}{2} \quad \text{and} \quad \dot{x}_a = \frac{\dot{y}_d}{2\tan\phi} \tag{4}$$

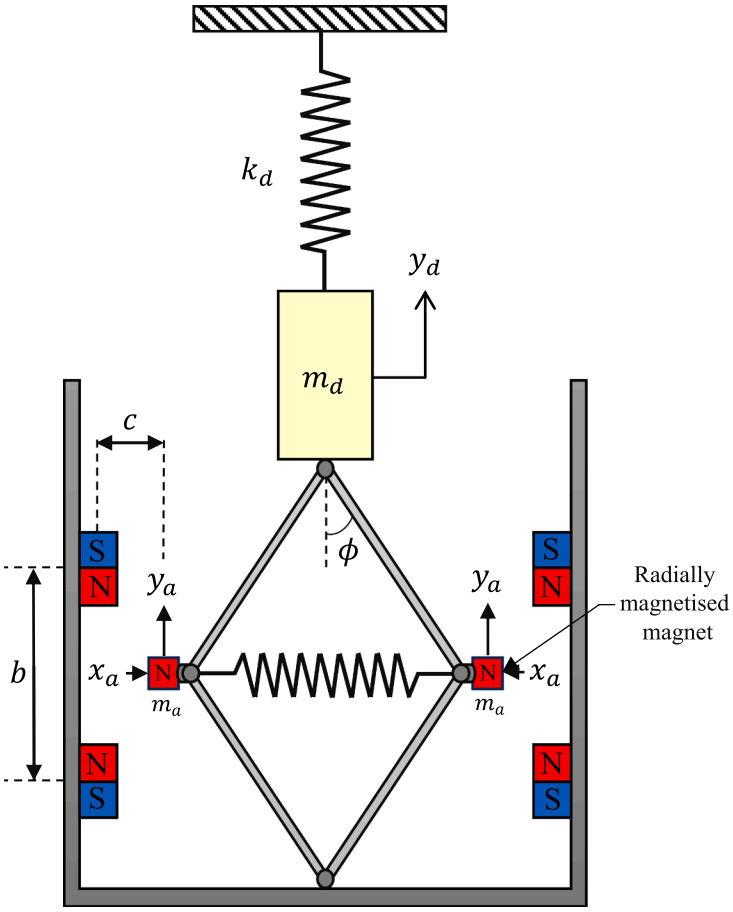

Fig. 1. The schematic diagram of elastomagnetic amplifier.

The kinetic energy of the central mass is derived as

$$T_d = \frac{1}{2} m_d \dot{y}_d^2 \tag{5}$$

The total kinetic energy of the amplifier magnet mass is derived as

$$T_a = \frac{1}{2} m_a \left(\dot{x}_a^2 + \dot{y}_a^2 \right) \tag{6}$$

Eq. (4) is substituted in Eq. (6). Accordingly, the total kinetic energy of the amplifier magnet mass is derived as

$$T_a = \frac{1}{2} m_a \dot{y}_d^2 \left(\frac{1}{4} + \frac{1}{4 \tan^2 \phi} \right) \tag{7}$$

The total kinetic energy of the elastomagnetic amplifier is derived as

$$\begin{aligned} T &= \frac{1}{2} \left(m_d + \frac{1}{2} m_a + \frac{m_a}{2 \tan^2 \phi} \right) \dot{y}_d^2 \\ &= \frac{1}{2} \left(m_d + \frac{m_a}{2 \sin^2 \phi} \right) \dot{y}_d^2 \end{aligned} \tag{8}$$

Simultaneously, the total potential energy of the elastomagnetic amplifier is derived as

$$V = \frac{1}{2} \left(k_d + k_a \cot^2 \phi \right) y_d^2 + V_m \tag{9}$$

where V_m defines the magnetic potential energy. Each wall contributes the total of the interactions with its two fixed magnets, and the magnetic interaction energy is additive. The factor of two results from the identical contributions from both walls due to geometric left-right symmetry. Therefore, V_m is derived as

$$V_m = 2\alpha \left(\left(\frac{1}{r^+} \right)^2 + \left(\frac{1}{r^-} \right)^2 \right) \tag{10}$$

The amplifier magnet and the fixed magnets on the left and right walls have the same distances because of the system's geometric left-right symmetry, i.e., $r_L^{\pm} = r_R^{\pm} = r^{\pm}$. Eq. (10) substitutes in Eq. (9). As a result, the total potential energy of the elastomagnetic amplifier is derived as

$$V = \frac{1}{2}\left(k_d + k_a \cot^2\phi\right) y_d^2 + 2\alpha\left(\left(\frac{1}{r^+}\right)^2 + \left(\frac{1}{r^-}\right)^2\right) \tag{11}$$

where α defines the magnetic strength coefficient. The Lagrange equation is employed to derive the governing equation of motion of the elastomagnetic amplifier, which is expressed as

$$L = T - V \tag{12}$$

The governing equation of motion is obtained by applying Euler-Lagrange's equation with respect to the generalised coordinate y_d and expressed as

$$\frac{d}{dt}\left(\frac{\partial L}{\partial \dot{y}_d}\right) - \frac{\partial L}{\partial y_d} = 0 \tag{13}$$

Eqs. (8) and (11) are substituted in Eq. (13). Accordingly, the governing equation of motion is derived as

$$\begin{aligned} &\left(m_d + \frac{m_a}{2\sin^2(\phi)}\right)\ddot{y}_d + \left(k_d + k_a\left(\cot^2(\phi)\right)\right) y_d \\ &+2\alpha\left(-\frac{\frac{y_d}{2\tan(\phi)}+c}{\tan(\phi)} + \frac{\frac{y_d}{2}+\frac{b}{2}}{\left(\left(\frac{y_d}{2\tan(\phi)}+c\right)^2+\left(\frac{y_d}{2}+\frac{b}{2}\right)^2\right)^2} - \frac{\frac{y_d}{2\tan(\phi)}+c}{\left(\left(\frac{y_d}{2\tan(\phi)}+c\right)^2+\left(\frac{y_d}{2}-\frac{b}{2}\right)^2\right)^2}\right) = 0 \end{aligned} \tag{14}$$

Eq. (14) is expanded using the Taylor series expansion around the equilibrium position $y = 0$. Accordingly, the expanded expression is derived as

$$\underbrace{\left(m_d + \frac{m_a}{2\sin^2\phi}\right)}_{m_b}\ddot{y}_d + \underbrace{\left(k_d + k_a\cot^2\phi\right)}_{k_b} y_d - A_0 - A_1 y_d + A_2 y_d^2 + A_3 y_d^3 + O\left(y_d^4\right) = 0 \tag{15}$$

where A_0, A_1, A_2, and A_3 are derived as

$$A_0 = \frac{128\alpha c\Theta}{\left(b^2+4c^2\right)^2} \quad \text{and} \quad \Theta = \frac{1}{2\tan\phi} \tag{16}$$

$$A_1 = \frac{32\alpha\left(4b^2\Theta^2 - 48c^2\Theta^2 - 3b^2 + 4c^2\right)}{\left(b^2+4c^2\right)^3} = \nu k_b \tag{17}$$

$$A_2 = \frac{3072c\left(\left(-4\Theta^2+1\right)c^2 + b^2\left(\Theta^2 - \frac{5}{4}\right)\right)\Theta\alpha}{\left(b^2+4c^2\right)^4} = \beta k_b \tag{18}$$

$$A_3 = \frac{1024\alpha\left(\begin{array}{c}\left(\Theta^4 - \frac{5}{2}\Theta^2 + \frac{5}{16}\right)b^4 - 40c^2\left(\Theta^4 - \frac{19}{10}\Theta^2 + \frac{1}{16}\right)b^2 \\ +80c^4\left(\Theta^4 - \frac{1}{2}\Theta^2 + \frac{1}{80}\right)\end{array}\right)}{\left(b^2+4c^2\right)^5} = \lambda k_b \tag{19}$$

where $\nu = A_1/k_b$ defines the ratio of magnetic linear stiffness to damper effective stiffness or magnetic stiffness ratio. $\beta = A_2/k_b$ and $\lambda = A_3/k_b$ define the ratio of squared and cubic stiffness to damper effective stiffness. Since the higher-order terms $O(y_d^4)$ represent insignificant nonlinearities that have little effect on the dynamic response during small amplitude vibrations around the equilibrium position, they are neglected. In addition, A_0 is a constant force that only modifies the static equilibrium position and has no effect on the dynamic response when vibrations are measured around equilibrium and is therefore neglected. Therefore, the final governing equation of motion is derived as

$$m_b\ddot{y}_d + (1-\nu)k_b y_d + A_2 y_d^2 + A_3 y_d^3 = 0 \tag{20}$$

The magnetic interaction between the stationary magnets on the walls and the moving amplifier magnets is the source of the negative stiffness, denoted by the term in the equation. This result reduces the system's net stiffness, lowering the resonant frequency and enabling the amplifier to greatly increase vibration amplitudes for more effective energy mitigation.

The effective mass and stiffness are evaluated by comparing with the static mass and stiffness of the elastomagnetic amplifiers to assess the advancement over the conventional mass-spring damper. Therefore, the effective mass ratio of the elastomagnetic amplifier with respect to the static mass is derived as

$$\gamma_b = \frac{m_b}{m_d} = \left(1 + \frac{\mu_a}{2\sin^2\phi}\right) \tag{21}$$

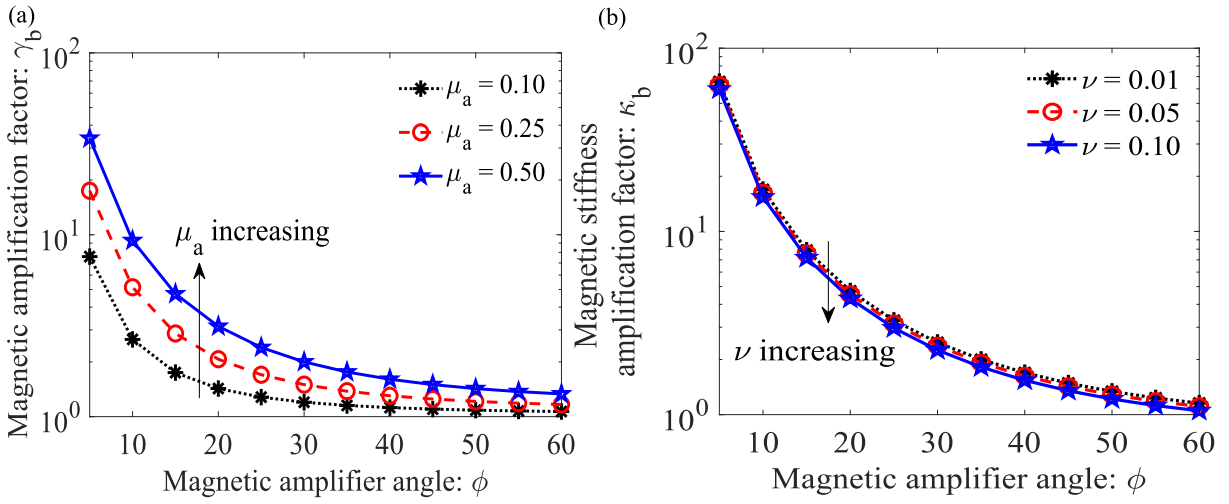

Fig. 2. (a) The variations of magnetic amplification factor versus magnetic amplifier angle for different values of amplifier to damper mass ratio. (b) The variations of magnetic stiffness amplification factor versus magnetic amplifier angle for different values of magnetic stiffness ratio.

where γ_b also defines the magnetic amplification factor. $\mu_a = m_a/m_d$ defines the amplifier-to-damper mass ratio. A_1 has a greater influence than A_2 and A_3 on the static stiffness of the amplifier in terms of restoring force generation process. Therefore, A_2 and A_3 are neglected to estimate effective stiffness. The effective stiffness ratio is derived as

$$\kappa_b = (1-\nu)\frac{\left(k_d + k_a \cot^2\phi\right)}{k_d} = (1-\nu)\left(1+\kappa\cot^2\phi\right) \tag{22}$$

where κ_b also defines the effective stiffness amplification factor. $\kappa = k_a/k_d$ defines the amplifier stiffness ratio. The magnetic force provides effective negative stiffness, which helps to increase the time period of the hosting structure during vibration. In other words, this effective stiffness provides advanced vibration reduction capacity to the amplifier. Fig. 2 shows how design parameters affect the elastomagnetic amplifier's performance metrics, particularly the magnetic amplification factor and the magnetic stiffness amplification factor. The device's ability to reduce vibrations beyond what traditional mass-spring-damper devices can do is largely dependent on these characteristics.

As the magnetic amplifier angle ϕ lowers, Fig. 2(a) demonstrates that the magnetic amplification factor, which is the ratio of the effective mass to the static damper mass ($\gamma_b = m_b/m_d$), rises sharply. In terms of physics, this indicates that a relatively modest physical mass m_a can behave as a significantly larger effective mass m_b at a smaller angle. Increasing the amplifier-to-damper mass ratio (μ_a) further amplifies this impact by enabling the device to better utilise inertial forces for vibration suppression without adding undue physical weight to the structure. A similar pattern can be seen in Fig. 2(b) for the magnetic stiffness amplification factor, which rises as the magnetic stiffness ratio ν rises and the amplifier angle ϕ falls. The creation of negative stiffness via magnetic contact is where this factor's physical relevance lies. By supplying this negative stiffness, the amplifier lowers the system's net stiffness, lowering the resonance frequency and lengthening the hosting structure's time period. In comparison to conventional passive dampers, this enables the amplifier to experience greater vibration amplitudes, dissipating more energy and offering better vibration reduction. These trends highlight that the amplifier operates most effectively within a lower range of ϕ, where both inertial and stiffness amplification mechanisms are dominant. The combined effect of mass amplification and negative stiffness enhances the dynamic interaction between the damper and the primary structure, leading to improved energy transfer and dissipation. This behaviour demonstrates the capability of the proposed mechanism to achieve enhanced vibration mitigation without increasing physical mass, while maintaining flexibility in tuning through μ_a and ν.

3. Elastomagnetic amplifier friction dampers

A building is conceptualised as a single degree of freedom (SDOF) system. The elastomagnetic amplifier friction damper (EAFD) is installed at the top of the SDOF system and the coupled system is shown in Fig. 3.

The energy method is applied to derive the governing equations of motion of the SDOF system controlled by the EAFD. Accordingly, the governing equation of motion is derived as

$$\begin{aligned} &m_s\ddot{u}_s + c_s\dot{u}_s + k_s u_s - \mu m_b g\,\mathrm{sgn}(\dot{u}_d) - c_b\dot{u}_d - k_b u_d + A_1 u_d - A_2 u_d^2 - A_3 u_d^3 = -m_s\ddot{u}_g \\ &m_b\ddot{u}_d + m_b\ddot{u}_s + \mu m_b g\,\mathrm{sgn}(\dot{u}_d) + c_b\dot{u}_d + k_b u_d - A_1 u_d + A_2 u_d^2 + A_3 u_d^3 = -m_b\ddot{u}_g \end{aligned} \tag{23}$$

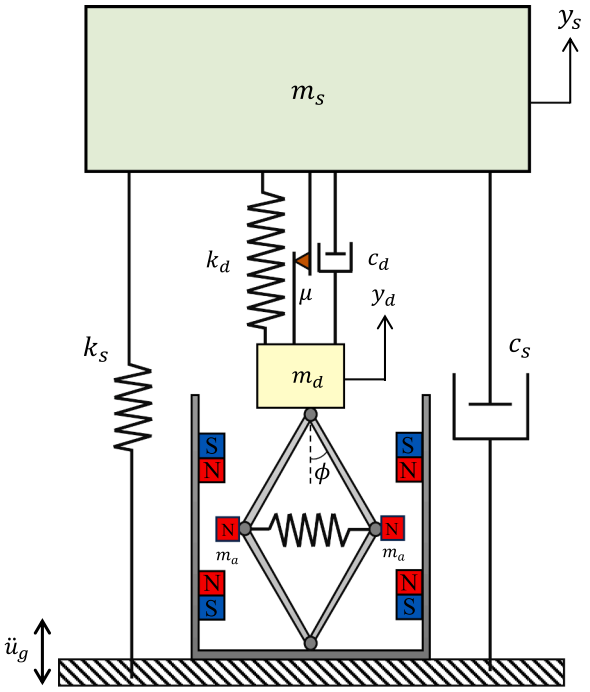

Fig. 3. A single degree of freedom system is controlled by elastomagnetic amplifier damper subjected to base excitation.

where $u_s = y_s - u_g$ and $u_d = y_d - y_s$ define the relative displacements of SDOF system and damper. $\ddot{u}_g$ defines the base excitation. μ defines the friction coefficient. m_s, $c_s = 2m_s\xi_s\omega_s$, and $k_s = m_s\omega_s^2$ define the mass, damping, and stiffness of the SDOF system. m_b, $c_b = 2m_b\xi_d\omega_d$, and k_b define the effective mass, damping, and stiffness of the EAFD. Eq. (23) is a highly nonlinear equation. The dynamic responses are derived using the harmonic balance method. However, before performing this method, the governing parameters of the EAFD need to be optimised to achieve robust vibration reduction. H_2 and H_∞ methods are employed to derive optimal design parameters in terms of closed-form expressions. The feasibility of the H_2 and H_∞- optimised parameters will be compared more closely with the optimal parameters derived from numerical methods. In addition, Eq. (23) is linearised to implement these methods, and the damping ratio of the SDOF system is assumed to be zero, i.e., $\xi_s = 0$. The statistical linearisation method is applied to Eq. (23) and the linearised parameters are derived as

$$c_e = E\left\{\frac{\partial\left(\mu m_b g\,\mathrm{sgn}(\dot{u}_d)\right)}{\partial\dot{u}_d}\right\} = \sqrt{\frac{2}{\pi}}\frac{\mu m_b g}{\sigma_{\dot{u}_d}} \tag{24}$$

The variance of the velocity response of the EAFD is denoted by $\sigma_{\dot{u}_d}$. An error arises during the linearisation process and is expressed as

$$\epsilon_b = \mu m_b g\,\mathrm{sgn}(\dot{u}_d) - c_e\dot{u}_d \quad \text{and} \quad \frac{\partial\epsilon_b^2}{\partial c_e} = E\left\{\left(\mu m_b g\,\mathrm{sgn}(\dot{u}_d) - c_e\dot{u}_d\right)^2\right\} = 0 \tag{25}$$

Eq. (25) indicates that the expected linearisation error is zero. The nonlinear restoring forces through the magnets are linearised as

$$A_{2e} = E\left\{\frac{\partial\left(A_2u_d^2\right)}{\partial u_d}\right\} = 0 \quad \text{and} \quad A_{3e} = E\left\{\frac{\partial\left(A_3u_d^3\right)}{\partial u_d}\right\} = 3A_3\sigma_{u_d}^2 \tag{26}$$

The standard deviation of the dynamic response of the damper is denoted by $\sigma_{u_d}^2$. The linearised terms are substituted in Eq. (23). In addition, the closed-form expressions for $\sigma_{\dot{u}_d}$ and $\sigma_{u_d}^2$ need to be derived using H_2 optimisation technique. To perform this method, the initial values of these quantities are considered zero and Eq. (23) is rewritten as

$$\begin{aligned} &m_s\ddot{u}_s + c_s\dot{u}_s + k_su_s - c_b\dot{u}_d - k_bu_d + \nu k_bu_d = -m_s\ddot{u}_g \\ &m_b\ddot{u}_d + m_b\ddot{u}_s + c_b\dot{u}_d + k_bu_d - \nu k_bu_d = -m_b\ddot{u}_g \end{aligned} \tag{27}$$

The steady state solutions are considered as $u_s = U_se^{i\omega t}$, $u_d = U_de^{i\omega t}$, and $\ddot{u}_g = U_ge^{i\omega t}$. These solutions are substituted in Eq. (27) to derive the transfer matrix. In addition, Eq. (27) is divided by m_s and the transfer matrix is expressed as

$$\begin{bmatrix} 2q\xi_s\omega_s + q^2 + \omega_s^2 & A_{12} \\ q^2\left(1 + \frac{\mu_a(\csc^2(\phi))}{2}\right)\mu_d & A_{22} \end{bmatrix}\begin{Bmatrix} U_s \\ U_d \end{Bmatrix} = \begin{bmatrix} -1 \\ -\left(1 + \frac{\mu_a(\csc^2(\phi))}{2}\right)\mu_d \end{bmatrix}U_g \tag{28}$$

$$A_{12} = \mu_d \begin{pmatrix} -\mu_a q\left(\csc^2(\phi)\right)\xi_d\omega_d + \kappa\left(\cot^2(\phi)\right)\omega_d^2\nu \\ -\kappa\left(\cot^2(\phi)\right)\omega_d^2 + \omega_d^2\nu - 2q\xi_d\omega_d - \omega_d^2 \end{pmatrix} \tag{29}$$

$$A_{22} = \mu_d \begin{pmatrix} \mu_a q\left(\csc^2(\phi)\right)\xi_d\omega_d + \frac{\mu_a q^2\left(\csc^2(\phi)\right)}{2} + \kappa\left(\cot^2(\phi)\right)\omega_d^2 \\ -\kappa\left(\cot^2(\phi)\right)\omega_d^2\nu - \omega_d^2\nu + \omega_d^2 + 2q\xi_d\omega_d + q^2 \end{pmatrix} \tag{30}$$

where $q = \mathrm{i}\omega$ and $\mathrm{i} = \sqrt{-1}$ denotes the imaginary unit. ω defines the excitation frequency. $\kappa = k_a/k_d$ defines the amplifier stiffness ratio. $\mu_a = m_a/m_d$ defines the amplifier-to-damper mass ratio. $\mu_d = m_d/m_s$ defines the ratio of damper mass to structural mass. The damping ratio of the main structure is considered zero, i.e., $\xi_s = 0$, to perform the optimisation schemes. Accordingly, the transfer function of the dynamic response of the main structure is derived as

$$H_s(q) = \left.\frac{U_s}{U_g}\right|_{q=\mathrm{i}\omega} = \frac{\begin{pmatrix} -\omega_d^2\mu_d\left(\csc^2(\phi)\right)\left(\cot^2(\phi)\right)\kappa\mu_a\nu + \omega_d\mu_d\left(\csc^4(\phi)\right)\mu_a^2 q\xi_d \\ +\omega_d^2\mu_d\left(\csc^2(\phi)\right)\left(\cot^2(\phi)\right)\kappa\mu_a - 2\omega_d^2\mu_d\left(\cot^2(\phi)\right)\kappa\nu \\ +2q^2 - \omega_d^2\mu_d\left(\csc^2(\phi)\right)\mu_a\nu + 4\omega_d\mu_d\left(\csc^2(\phi)\right)\mu_a q\xi_d \\ +\omega_d^2\mu_d\left(\csc^2(\phi)\right)\mu_a + 2\omega_d^2\mu_d\left(\cot^2(\phi)\right)\kappa - 2\kappa\left(\cot^2(\phi)\right)\omega_d^2\nu \\ +2\mu_a q\left(\csc^2(\phi)\right)\xi_d\omega_d + 2\kappa\left(\cot^2(\phi)\right)\omega_d^2 + \mu_a q^2\left(\csc^2(\phi)\right) \\ -2\omega_d^2\mu_d\nu + 4\omega_d\mu_d q\xi_d + 2\omega_d^2\mu_d - 2\omega_d^2\nu + 4q\xi_d\omega_d + 2\omega_d^2 \end{pmatrix}}{\Delta} \tag{31}$$

The transfer function of the dynamic response of the damper is derived as

$$H_d(q) = \left.\frac{U_d}{U_g}\right|_{q=\mathrm{i}\omega} = \frac{-\omega_s^2\left(\left(\csc^2(\phi)\right)\mu_a + 2\right)}{\Delta} \tag{32}$$

The denominator of Eqs. (31) and (32) is derived as

$$\Delta = \begin{matrix} \left(\csc^2(\phi)\right)\mu_a q^2\omega_s^2 + 2\left(\cot^2(\phi)\right)\kappa\, q^2\omega_d^2 + 2\left(\cot^2(\phi)\right)\kappa\,\omega_d^2\omega_s^2 + 2q^4 + 2q^2\omega_d^2 \\ +2\omega_d^2\omega_s^2 + 2q^2\omega_s^2 + 2\mu_d q^2\omega_d^2 - \left(\csc^2(\phi)\right)\left(\cot^2(\phi)\right)\kappa\mu_a\mu_d\nu\, q^2\omega_d^2 - 2\nu\, q^2\omega_d^2 \\ -2\nu\,\omega_d^2\omega_s^2 + 4q^3\xi_d\omega_d + \left(\csc^2(\phi)\right)\mu_a q^4 - 2\mu_d\nu\, q^2\omega_d^2 + 4\mu_d q^3\xi_d\omega_d + 4q\xi_d\omega_d\omega_s^2 \\ +\left(\csc^2(\phi)\right)\mu_a\mu_d q^2\omega_d^2 + 2\left(\csc^2(\phi)\right)\mu_a q^3\xi_d\omega_d + 2\left(\cot^2(\phi)\right)\kappa\mu_d q^2\omega_d^2 \\ -2\left(\cot^2(\phi)\right)\kappa\nu\, q^2\omega_d^2 - 2\left(\cot^2(\phi)\right)\kappa\nu\,\omega_d^2\omega_s^2 + \mu_d\left(\csc^4(\phi)\right)\mu_a^2 q^3\xi_d\omega_d \\ -\left(\csc^2(\phi)\right)\mu_a\mu_d\nu\, q^2\omega_d^2 + 4\left(\csc^2(\phi)\right)\mu_a\mu_d q^3\xi_d\omega_d - 2\left(\cot^2(\phi)\right)\kappa\mu_d\nu\, q^2\omega_d^2 \\ +2\left(\csc^2(\phi)\right)\mu_a q\xi_d\omega_d\omega_s^2 + \left(\csc^2(\phi)\right)\left(\cot^2(\phi)\right)\kappa\mu_a\mu_d q^2\omega_d^2 \end{matrix} \tag{33}$$

Eqs. (31) and (33) are employed further to perform the optimisation H_2 and H_∞ schemes. In addition, Eq. (32) is also employed to derive the standard deviation of the dynamic response and velocity response of the damper.

4. Optimal design parameter

The H_2 optimisation scheme is applied under white-noise random excitation, whereas the H_∞ optimisation is employed under harmonic excitation. Later, both excitations are applied to estimate the dynamic responses of the controlled structures.

4.1. H_2 optimisation

Eqs. (31) and (33) are employed to derive the standard deviation of the dynamic response of the structure and is expressed as

$$\sigma_{u_s}^2 = \frac{S_0\pi\left(\ N_1\ \right)}{4\omega_s^6\mu_d\omega_d\left(2\left(\sin^2(\phi)\right) + \mu_a\right)^3\xi_d} \tag{34}$$

The closed-form expression for N_1 is derived and expressed in A. In addition, the standard deviation of the dynamic response of the damper is derived as

$$\sigma_{u_d}^2 = \frac{4S_0\pi\begin{pmatrix} \left(\kappa\,\omega_d^2\left(\mu_d+1\right)^2(\nu-1)\left(\cot^2(\phi)\right) + \left(\mu_d+1\right)^2(\nu-1)\omega_d^2 - \omega_s^2\mu_d\right)\left(\sin^2(\phi)\right) \\ +\mu_a\mu_d\begin{pmatrix} \kappa\,\omega_d^2\left(\mu_d+1\right)(\nu-1)\left(\cot^2(\phi)\right) + \frac{\mu_a\left(\mu_d(\nu-1)\omega_d^2-\omega_s^2\right)\left(\csc^2(\phi)\right)}{4} \\ +\frac{\kappa\mu_a\mu_d\omega_d^2(\nu-1)\left(\cot^2(\phi)\right)}{4} + \left(\mu_d+1\right)(\nu-1)\omega_d^2 - \omega_s^2 \end{pmatrix} \end{pmatrix}}{4\omega_d^3\mu_d\xi_d\omega_s^2(\nu-1)\left(\left(\cot^2(\phi)\right)\kappa+1\right)\left(2\left(\sin^2(\phi)\right)+\mu_a\right)} \tag{35}$$

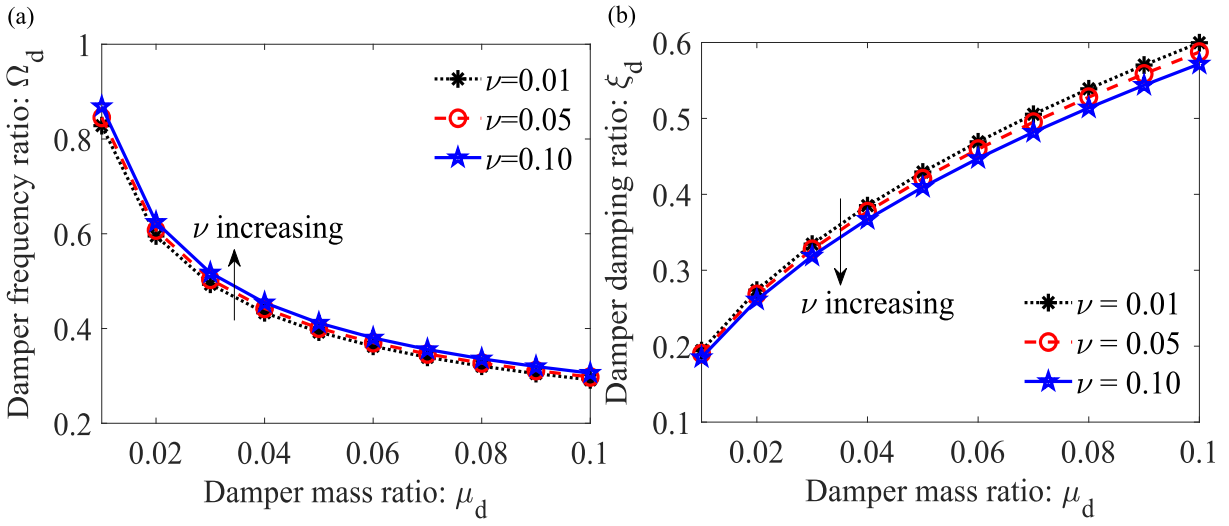

Fig. 4. The variations of the optimal (a) frequency and (b) damping ratios of the damper versus damper mass ratio for different values of magnetic stiffness ratio.

The standard deviation of the velocity response of the damper is derived as

$$\sigma_{\dot{u}_d}^2 = \frac{S_0\pi\left(\left(2\mu_d+2\right)\left(\sin^2(\phi)\right)+\mu_a\mu_d\right)}{2\xi_d\omega_d\left(2\left(\sin^2(\phi)\right)+\mu_a\right)\mu_d} \tag{36}$$

The closed-form expressions for the optimal frequency and damping ratios of the damper are derived using the following expressions.

$$\frac{\partial\sigma_{\dot{u}_s}^2}{\partial\xi_d}=0 \quad \text{and} \quad \frac{\partial\sigma_{\dot{u}_s}^2}{\partial\omega_d}=0 \tag{37}$$

Eq. (34) is substituted in the first expression of Eq. (37). Accordingly, the closed-form expression for the damping ratio of the damper is derived as

$$\xi_d = \sqrt{\frac{N_2}{2\left(\left(2\mu_d+2\right)\left(\sin^2(\phi)\right)+\mu_a\mu_d\right)^3\left(\csc^4(\phi)\right)\left(2\left(\sin^2(\phi)\right)+\mu_a\right)^2\omega_d^2\omega_s^2}} \tag{38}$$

The closed-form expression for N_2 is derived and expressed in A. Eq. (38) is substituted in Eq. (34). As a result, the standard deviation of the dynamic response of the main structure is modified which only contains the natural frequency of the damper. This modified Eq. (34) is substituted in the second expression of the Eq. (37) to derive the optimal frequency of the damper. Therefore, the optimal frequency of the damper is derived as

$$\left(\omega_d\right)_{\text{opt}} = \sqrt{\frac{\left(\left(2\mu_d-4\right)\left(\sin^2(\phi)\right)+\mu_a\mu_d\right)\omega_s^2\left(2\left(\sin^2(\phi)\right)+\mu_a\right)}{2(\nu-1)\left(\left(\cot^2(\phi)\right)\kappa+1\right)\left(\left(2\mu_d+2\right)\left(\sin^2(\phi)\right)+\mu_a\mu_d\right)^2}} \tag{39}$$

The frequency ratio of the damper is derived as

$$\left(\Omega_d\right)_{\text{opt}} = \sqrt{\frac{\left(\left(2\mu_d-4\right)\left(\sin^2(\phi)\right)+\mu_a\mu_d\right)\left(2\left(\sin^2(\phi)\right)+\mu_a\right)}{2(\nu-1)\left(\left(\cot^2(\phi)\right)\kappa+1\right)\left(\left(2\mu_d+2\right)\left(\sin^2(\phi)\right)+\mu_a\mu_d\right)^2}} \tag{40}$$

Eq. (39) is substituted in Eq. (38) to derive the optimal damping ratio of the damper. Accordingly, the optimal damping ratio of the damper is derived as

$$\left(\xi_d\right)_{\text{opt}} = \sqrt{\frac{\mu_d\left(\sin^2(\phi)\right)\left(\left(2\mu_d-8\right)\left(\sin^2(\phi)\right)+\mu_a\mu_d\right)(1-\nu)\left(\left(\cot^2(\phi)\right)\kappa+1\right)}{4\left(\left(2\mu_d+2\right)\left(\sin^2(\phi)\right)+\mu_a\mu_d\right)\left(\left(2\mu_d-4\right)\left(\sin^2(\phi)\right)+\mu_a\mu_d\right)}} \tag{41}$$

The variations in the optimal frequency ratio of the damper are obtained by varying the damper mass ratio, as shown in Fig. 4 (a).

The magnetic stiffness ratio is also varied to identify the effect of magnets on the physical properties of the damper during vibration. It is observed that the damper frequency ratio decreases with increasing damper mass ratio, while it increases with the magnetic stiffness ratio. This behaviour indicates that higher mass ratios combined with lower magnetic stiffness lead to lower tuning frequencies, corresponding to an increased effective time period of the coupled system. Such a shift enables improved interaction between the damper and the primary structure, thereby enhancing vibration attenuation near resonance. To further assess the influence of the

magnetic amplifier, the variations of the damping ratio with the damper mass ratio are shown in Fig. 4(b). The optimal damping ratio increases with the damper mass ratio and decreases with increasing magnetic stiffness ratio, reflecting the need for greater energy dissipation as the effective inertia of the system increases. These results suggest that an appropriate combination of higher damper mass ratio and moderate magnetic stiffness can improve overall vibration mitigation performance while maintaining stable system behaviour.

4.2. H_∞ optimisation

In addition to the H_2 optimisation method, H_∞ optimisation scheme is employed to obtain the optimal design parameters under harmonic excitation. Accordingly, Eq. (28) is further divided by ω_s^2 to perform the H_∞ optimisation scheme. The transfer matrix is derived as

$$\begin{bmatrix} 2\,\mathrm{i}\Omega\xi_s - \Omega^2 + 1 & A_{12} \\ \left(-\frac{\mu_a\Omega^2(\csc^2(\phi))}{2} - \Omega^2\right)\mu_d & A_{22} \end{bmatrix} \begin{Bmatrix} U_s \\ U_d \end{Bmatrix} = \begin{bmatrix} -1 \\ -\left(1 + \frac{\mu_a(\csc^2(\phi))}{2}\right)\mu_d \end{bmatrix} \frac{U_g}{\omega_s^2} \tag{42}$$

The closed-form expressions for A_{12} and A_{22} are derived as

$$\begin{aligned} A_{12} &= \kappa\mu_d\left(\cot^2(\phi)\right)\Omega_d^2(-1+\nu) - \mathrm{i}\mu_a\left(\csc^2(\phi)\right)\xi_d\Omega\Omega_d\mu_d + \mu_d(-1+\nu)\Omega_d^2 - 2\,\mathrm{i}\Omega_d\xi_d\Omega\mu_d \\ A_{22} &= \left(\mu_a\left(\mathrm{i}\xi_d\Omega_d - \frac{\Omega}{2}\right)\Omega\left(\csc^2(\phi)\right) - \Omega_d^2\kappa\left(\cot^2(\phi)\right)(-1+\nu) + (1-\nu)\Omega_d^2 + 2\,\mathrm{i}\Omega_d\xi_d\Omega - \Omega^2\right)\mu_d \end{aligned} \tag{43}$$

The damping of the main structure is considered zero, i.e., $\xi_s = 0$. Accordingly, the transfer function of the dynamic response of the main structure is derived as

$$\begin{aligned} H_s(\Omega) &= \left(\frac{U_s}{U_g}\right)\omega_s^2 \\ &= \frac{\begin{array}{c} -\mu_d\Omega_d^2\left(\csc^2(\phi)\right)\left(\cot^2(\phi)\right)\kappa\mu_a\nu + \mu_d\Omega_d^2\left(\csc^2(\phi)\right)\left(\cot^2(\phi)\right)\kappa\mu_a \\ -\mu_d\Omega_d^2\left(\csc^2(\phi)\right)\mu_a\nu - 2\mu_d\kappa\left(\cot^2(\phi)\right)\Omega_d^2\nu + \mu_d\Omega_d^2\left(\csc^2(\phi)\right)\mu_a \\ +2\mu_d\kappa\left(\cot^2(\phi)\right)\Omega_d^2 - 2\kappa\left(\cot^2(\phi)\right)\Omega_d^2\nu - \mu_a\Omega^2\left(\csc^2(\phi)\right) \\ +2\kappa\left(\cot^2(\phi)\right)\Omega_d^2 - 2\mu_d\Omega_d^2\nu + 2\mu_d\Omega_d^2 - 2\Omega_d^2\nu - 2\Omega^2 + 2\Omega_d^2 \\ +\mathrm{i}\left(\begin{array}{c} \mu_d\Omega_d\left(\csc^4(\phi)\right)\Omega\,\mu_a^2\xi_d + 4\Omega\xi_d\Omega_d \\ +4\mu_d\mu_a\Omega\xi_d\Omega_d\left(\csc^2(\phi)\right) + 4\Omega_d\xi_d\Omega\mu_d + 2\mu_a\Omega\left(\csc^2(\phi)\right)\xi_d\Omega_d \end{array}\right) \end{array}}{\Delta} \end{aligned} \tag{44}$$

The transfer function of the dynamic response of the damper is derived as

$$H_d(\Omega) = \left(\frac{U_d}{U_g}\right)\omega_s^2 = \frac{\mu_a\left(\csc^2(\phi)\right) + 2}{\Delta} \tag{45}$$

The denominator of Eqs. (44) and (45) is derived as

$$\begin{aligned} \Delta = &\begin{array}{c} 2\Omega^2\Omega_d^2 + 2\mu_d\left(\cot^2(\phi)\right)\Omega^2\kappa\,\Omega_d^2 + 2\Omega_d^2\nu - 2\left(\cot^2(\phi)\right)\Omega^2\kappa\nu\,\Omega_d^2 \\ +\left(\csc^2(\phi)\right)\Omega^2\mu_a\mu_d\Omega_d^2 - \left(\csc^2(\phi)\right)\left(\cot^2(\phi)\right)\Omega^2\kappa\mu_a\mu_d\nu\,\Omega_d^2 \\ +\mu_a\Omega^2\left(\csc^2(\phi)\right) + 2\Omega^2 + \left(\csc^2(\phi)\right)\left(\cot^2(\phi)\right)\Omega^2\kappa\mu_a\mu_d\Omega_d^2 \\ -2\mu_d\Omega^2\nu\,\Omega_d^2 + 2\kappa\left(\cot^2(\phi)\right)\Omega_d^2\nu + 2\left(\cot^2(\phi)\right)\Omega^2\kappa\,\Omega_d^2 \\ -2\mu_d\left(\cot^2(\phi)\right)\Omega^2\kappa\nu\,\Omega_d^2 - 2\Omega^4 - 2\Omega_d^2 - \left(\csc^2(\phi)\right)\Omega^2\mu_a\mu_d\nu\,\Omega_d^2 \\ -2\kappa\left(\cot^2(\phi)\right)\Omega_d^2 - \left(\csc^2(\phi)\right)\Omega^4\mu_a + 2\mu_d\Omega^2\Omega_d^2 - 2\Omega^2\nu\,\Omega_d^2 \end{array} \\ &+\mathrm{i}\left(\begin{array}{c} 4\mu_d\Omega^3\xi_d\Omega_d + 4\mu_d\left(\csc^2(\phi)\right)\Omega^3\mu_a\xi_d\Omega_d + \left(\csc^4(\phi)\right)\Omega^3\mu_a^2\mu_d\xi_d\Omega_d \\ +4\Omega^3\xi_d\Omega_d - 4\Omega_d\xi_d\Omega - 2\mu_a\Omega\left(\csc^2(\phi)\right)\xi_d\Omega_d + 2\left(\csc^2(\phi)\right)\Omega^3\mu_a\xi_d\Omega_d \end{array}\right) \end{aligned} \tag{46}$$

The resultant of Eq. (44) is written as

$$|H_s(\Omega)| = \left|\frac{I_1}{I_2}\right|\sqrt{\frac{\frac{R_1^2}{I_1^2} + \xi_d^2}{\frac{R_2^2}{I_2^2} + \xi_d^2}} \tag{47}$$

H_∞ optimisation is employed. Accordingly, the constraints are derived as

$$\left|\frac{R_1}{I_1}\right|_\Omega = \left|\frac{R_2}{I_2}\right|_\Omega \quad \text{and} \quad \left|\frac{I_1}{I_2}\right|_{\Omega_1} = \left|\frac{I_1}{I_2}\right|_{\Omega_2} \tag{48}$$

The first expression of Eq. (48) is applied, and an expression with the frequency ratio is derived as

$$\begin{pmatrix} -2\mu_d\left(\csc^4(\phi)\right)\mu_a^2 - 8\left(\csc^2(\phi)\right)\mu_a\mu_d - 4\left(\csc^2(\phi)\right)\mu_a - 8\mu_d - 8 \end{pmatrix}\Omega^4 + \begin{pmatrix} 8 + 4\mu_d - 8\Omega_d^2\nu + 16\mu_d\Omega_d^2 + 8\mu_d^2\Omega_d^2 + 8\Omega_d^2 - 16\mu_d\Omega_d^2\nu - 8\mu_d^2\nu\,\Omega_d^2 \\ -2\left(\csc^2(\phi)\right)\left(\cot^2(\phi)\right)\kappa\,\mu_a^2\mu_d^2\nu\,\Omega_d^2 - 4\left(\cot^2(\phi)\right)\left(\csc^2(\phi)\right)\kappa\mu_a\mu_d^2\nu\,\Omega_d^2 \\ -4\mu_d\Omega_d^2\left(\csc^2(\phi)\right)\left(\cot^2(\phi)\right)\kappa\mu_a\nu - 4\mu_d\Omega_d^2\kappa\mu_a\nu\left(\cot^2(\phi)\right) \\ +2\left(\csc^2(\phi)\right)\left(\cot^2(\phi)\right)\kappa\,\mu_a^2\mu_d^2\Omega_d^2 + 4\left(\cot^2(\phi)\right)\left(\csc^2(\phi)\right)\kappa\mu_a\mu_d^2\Omega_d^2 \\ -4\left(\cot^2(\phi)\right)\kappa\mu_a\mu_d^2\nu\,\Omega_d^2 + 4\mu_d\Omega_d^2\left(\csc^2(\phi)\right)\left(\cot^2(\phi)\right)\kappa\mu_a \\ +16\mu_d\kappa\left(\cot^2(\phi)\right)\Omega_d^2 + 8\mu_d\Omega_d^2\left(\csc^2(\phi)\right)\mu_a - 8\kappa\left(\cot^2(\phi)\right)\Omega_d^2\nu \\ +2\left(\csc^4(\phi)\right)\mu_a^2\mu_d^2\Omega_d^2 + 8\left(\cot^2(\phi)\right)\kappa\,\mu_d^2\Omega_d^2 + 8\left(\csc^2(\phi)\right)\mu_a\mu_d^2\Omega_d^2 \\ -16\mu_d\kappa\left(\cot^2(\phi)\right)\Omega_d^2\nu - 8\mu_d\Omega_d^2\left(\csc^2(\phi)\right)\mu_a\nu + 4\mu_d\Omega_d^2\kappa\mu_a\left(\cot^2(\phi)\right) \\ -2\left(\csc^4(\phi)\right)\mu_a^2\mu_d^2\nu\,\Omega_d^2 - 8\left(\cot^2(\phi)\right)\kappa\,\mu_d^2\nu\,\Omega_d^2 - 8\left(\csc^2(\phi)\right)\mu_a\mu_d^2\nu\,\Omega_d^2 \\ +4\left(\cot^2(\phi)\right)\kappa\mu_a\mu_d^2\Omega_d^2 + \mu_d\left(\csc^4(\phi)\right)\mu_a^2 + 4\left(\csc^2(\phi)\right)\mu_a\mu_d \\ +8\kappa\left(\cot^2(\phi)\right)\Omega_d^2 + 4\left(\csc^2(\phi)\right)\mu_a \end{pmatrix}\Omega^2 + \begin{pmatrix} +2\mu_d\Omega_d^2\left(\csc^2(\phi)\right)\left(\cot^2(\phi)\right)\kappa\mu_a\nu - 2\mu_d\Omega_d^2\left(\csc^2(\phi)\right)\left(\cot^2(\phi)\right)\kappa\mu_a \\ +2\mu_d\Omega_d^2\kappa\mu_a\nu\left(\cot^2(\phi)\right) + 8\mu_d\kappa\left(\cot^2(\phi)\right)\Omega_d^2\nu + 4\mu_d\Omega_d^2\left(\csc^2(\phi)\right)\mu_a\nu \\ -2\mu_d\Omega_d^2\kappa\mu_a\left(\cot^2(\phi)\right) - 8\mu_d\kappa\left(\cot^2(\phi)\right)\Omega_d^2 + 8\kappa\left(\cot^2(\phi)\right)\Omega_d^2\nu \\ -4\mu_d\Omega_d^2\left(\csc^2(\phi)\right)\mu_a - 8\kappa\left(\cot^2(\phi)\right)\Omega_d^2 + 8\mu_d\Omega_d^2\nu - 8\mu_d\Omega_d^2 + 8\Omega_d^2\nu \\ -8\Omega_d^2 = 0 \end{pmatrix} \tag{49}$$

The above expression is written as

$$\Omega^4 + \left(-\Omega_1^2 - \Omega_2^2\right)\Omega^2 + \Omega_1^2\Omega_2^2 = 0 \tag{50}$$

Eqs. (49) and (50) are compared.

$$\Omega_1^2 + \Omega_2^2 = \frac{\begin{pmatrix} 8 + 4\mu_d - 8\Omega_d^2\nu + 16\mu_d\Omega_d^2 + 8\mu_d^2\Omega_d^2 + 8\Omega_d^2 - 16\mu_d\Omega_d^2\nu - 8\mu_d^2\nu\,\Omega_d^2 \\ -2\left(\csc^2(\phi)\right)\left(\cot^2(\phi)\right)\kappa\,\mu_a^2\mu_d^2\nu\,\Omega_d^2 - 4\left(\cot^2(\phi)\right)\left(\csc^2(\phi)\right)\kappa\mu_a\mu_d^2\nu\,\Omega_d^2 \\ -4\mu_d\Omega_d^2\left(\csc^2(\phi)\right)\left(\cot^2(\phi)\right)\kappa\mu_a\nu - 4\mu_d\Omega_d^2\kappa\mu_a\nu\left(\cot^2(\phi)\right) \\ +2\left(\csc^2(\phi)\right)\left(\cot^2(\phi)\right)\kappa\,\mu_a^2\mu_d^2\Omega_d^2 + 4\left(\cot^2(\phi)\right)\left(\csc^2(\phi)\right)\kappa\mu_a\mu_d^2\Omega_d^2 \\ -4\left(\cot^2(\phi)\right)\kappa\mu_a\mu_d^2\nu\,\Omega_d^2 + 4\mu_d\Omega_d^2\left(\csc^2(\phi)\right)\left(\cot^2(\phi)\right)\kappa\mu_a \\ +16\mu_d\kappa\left(\cot^2(\phi)\right)\Omega_d^2 + 8\mu_d\Omega_d^2\left(\csc^2(\phi)\right)\mu_a - 8\kappa\left(\cot^2(\phi)\right)\Omega_d^2\nu \\ +2\left(\csc^4(\phi)\right)\mu_a^2\mu_d^2\Omega_d^2 + 8\left(\cot^2(\phi)\right)\kappa\,\mu_d^2\Omega_d^2 + 8\left(\csc^2(\phi)\right)\mu_a\mu_d^2\Omega_d^2 \\ -16\mu_d\kappa\left(\cot^2(\phi)\right)\Omega_d^2\nu - 8\mu_d\Omega_d^2\left(\csc^2(\phi)\right)\mu_a\nu + 4\mu_d\Omega_d^2\kappa\mu_a\left(\cot^2(\phi)\right) \\ -2\left(\csc^4(\phi)\right)\mu_a^2\mu_d^2\nu\,\Omega_d^2 - 8\left(\cot^2(\phi)\right)\kappa\,\mu_d^2\nu\,\Omega_d^2 - 8\left(\csc^2(\phi)\right)\mu_a\mu_d^2\nu\,\Omega_d^2 \\ +4\left(\cot^2(\phi)\right)\kappa\mu_a\mu_d^2\Omega_d^2 + \mu_d\left(\csc^4(\phi)\right)\mu_a^2 + 4\left(\csc^2(\phi)\right)\mu_a\mu_d \\ +8\kappa\left(\cot^2(\phi)\right)\Omega_d^2 + 4\left(\csc^2(\phi)\right)\mu_a \end{pmatrix}}{\begin{pmatrix} 2\mu_d\left(\csc^4(\phi)\right)\mu_a^2 + 8\left(\csc^2(\phi)\right)\mu_a\mu_d + 4\left(\csc^2(\phi)\right)\mu_a + 8\mu_d + 8 \end{pmatrix}} \tag{51}$$

The second expression of Eq. (48) is applied, and an expression with the frequency ratio is derived as

$$\Omega_1 + \Omega_2 = 0 \tag{52}$$

Eqs. (51) and (52) are equated and the closed-form expression for the optimal frequency ratio of the damper is derived as

$$\Omega_d = \sqrt{\frac{\mu_d\left(\csc^4(\phi)\right)\mu_a^2 + 4\left(\csc^2(\phi)\right)\mu_a\mu_d + 4\left(\csc^2(\phi)\right)\mu_a + 4\mu_d + 8}{\begin{matrix} 8 - 8\nu + 16\mu_d + 4\left(\csc^2(\phi)\right)\left(\cot^2(\phi)\right)\kappa\mu_a\mu_d - 4\left(\cot^2(\phi)\right)\kappa\mu_a\mu_d^2\nu \\ -4\left(\cot^2(\phi)\right)\kappa\mu_a\mu_d\nu + 2\left(\csc^2(\phi)\right)\left(\cot^2(\phi)\right)\kappa\,\mu_a^2\mu_d^2 + 8\left(\cot^2(\phi)\right)\kappa \\ +4\left(\csc^2(\phi)\right)\left(\cot^2(\phi)\right)\kappa\mu_a\mu_d^2 - 4\left(\csc^2(\phi)\right)\left(\cot^2(\phi)\right)\kappa\mu_a\mu_d\nu \\ -2\left(\csc^2(\phi)\right)\left(\cot^2(\phi)\right)\kappa\,\mu_a^2\mu_d^2\nu - 4\left(\csc^2(\phi)\right)\left(\cot^2(\phi)\right)\kappa\mu_a\mu_d^2\nu - 8\mu_d^2\nu \\ -16\mu_d\nu + 8\mu_d^2 - 8\left(\cot^2(\phi)\right)\kappa\nu + 2\left(\csc^4(\phi)\right)\mu_a^2\mu_d^2 + 8\left(\csc^2(\phi)\right)\mu_a\mu_d^2 \\ +8\left(\cot^2(\phi)\right)\kappa\,\mu_d^2 + 16\left(\cot^2(\phi)\right)\kappa\mu_d - 2\left(\csc^4(\phi)\right)\mu_a^2\mu_d^2\nu \\ -8\left(\csc^2(\phi)\right)\mu_a\mu_d^2\nu - 16\left(\cot^2(\phi)\right)\kappa\mu_d\nu - 8\left(\cot^2(\phi)\right)\kappa\,\mu_d^2\nu \\ -8\left(\csc^2(\phi)\right)\mu_a\mu_d\nu + 4\left(\cot^2(\phi)\right)\kappa\mu_a\mu_d^2 + 4\left(\cot^2(\phi)\right)\kappa\mu_a\mu_d \\ +8\left(\csc^2(\phi)\right)\mu_a\mu_d \end{matrix}}} \tag{53}$$

The roots of Ω_1^2 and Ω_2^2 are derived as

$$\Omega_{1,2}^2 = \pm\sqrt{\frac{2\left(\sin^2(\phi)\right)\left(\kappa\left(\cot^2(\phi)\right) + 1\right)(1-\nu)\Omega_d^2}{2\left(\sin^2(\phi)\right) + \mu_a}} \tag{54}$$

The optimal damping ratio of the damper is derived using the following expressions and is expressed as

$$\frac{\partial|H_s(\Omega)|^2}{\partial\Omega^2} = 0 \quad \text{and} \quad \xi_d = \sqrt{\frac{\xi_{d1}^2 + \xi_{d2}^2}{2}} \tag{55}$$

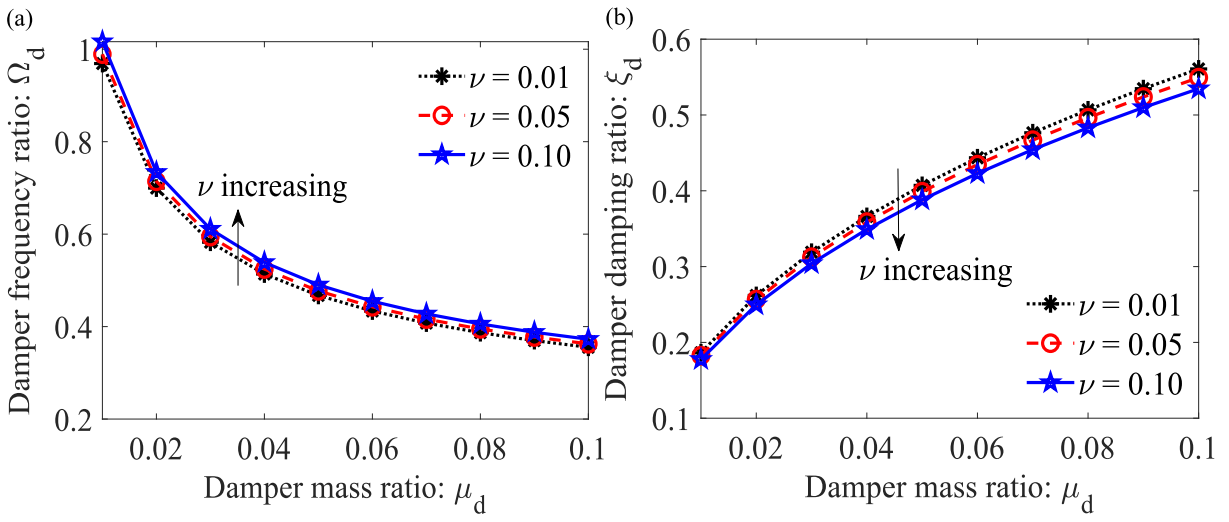

Fig. 5. The optimal (a) frequency and (b) damping ratios of the damper versus damper mass ratio for different values of magnetic stiffness ratio.

Eq. (44) is substituted in the first expression of Eq. (55). Accordingly, the closed-form expression for $\xi_{d1,d2}^2$ is derived as

$$Z_1\xi_{d1,d2}^4 + Z_2\xi_{d1,d2}^2 + Z_3 = 0$$
$$\xi_{d1,d2}^2 = \frac{-Z_2 \pm \sqrt{Z_2^2 - 4Z_1Z_3}}{2Z_1} \tag{56}$$

The closed-form expressions for Z_1, Z_2, and Z_3 are derived and expressed in B. Fig. 5(a) illustrates how the damper's optimal frequency ratios fluctuate depending on the damper mass ratio. The impact of magnets on the damper's physical characteristics during vibration is also determined by varying the magnetic stiffness ratio.

It is observed that the damper frequency ratio decreases with increasing damper mass ratio, while it increases with the magnetic stiffness ratio. This behaviour indicates that higher damper mass ratios combined with lower magnetic stiffness shift the optimal tuning towards lower frequencies, corresponding to an increased effective time period of the coupled system. Such a shift enhances the dynamic interaction between the damper and the primary structure, thereby improving vibration attenuation near resonance. To further examine the influence of the magnetic amplifier, the variations of the damping ratio with the damper mass ratio are presented in Fig. 5(b). The optimal damping ratio increases with the damper mass ratio and decreases with increasing magnetic stiffness ratio, reflecting the requirement for greater energy dissipation as the effective inertia of the system increases. This trend highlights the coupled role of inertia amplification and damping in stabilising the system response. Accordingly, an appropriate combination of higher damper mass ratio and moderate magnetic stiffness is desirable to achieve enhanced vibration mitigation while maintaining stable dynamic behaviour.

5. Dynamic response analysis

The effectiveness of the optimal design parameters is examined by evaluating the dynamic responses of the controlled structures. Furthermore, $\xi_s = 0.01$, or the damping ratio of the main structure, is taken to be 0.01.

5.1. Frequency domain response

At the base, harmonic excitation is applied first. In order to compare the innovative and conventional dampers in terms of vibration reduction, this paper considers H_2 and H_∞ optimised traditional tuned mass dampers. To ensure a fair comparison, the total static mass of each damper is kept constant. The total mass of the dampers is taken as 0.05. The amplifier stiffness ratio is considered 0.5. The magnetic stiffness ratio is considered 0.01. The magnetic amplifier angle is considered 10^o. The damping ratio of the SDOF systems is taken as 0.01. The conventional tuned mass dampers are denoted as TMD1 and TMD2. TMD1 is developed by Warburton [52] and Zilletti et al. [53] while TMD2 is developed by Iwata [54]. The frictional tuned mass damper (FTMD) is developed by Gewei and Basu [55]. The variations of structural displacements of the SDOF systems controlled by H_2 optimised dampers are shown in Fig. 6(a).

The displacement response of the uncontrolled structure is also evaluated, and the maximum displacement is obtained as 50. The displacement responses of the SDOF systems controlled by TMD1 and TMD2 are 8.0177 and 7.5055, respectively, while the EAFD-controlled system exhibits a significantly lower maximum displacement of 3.9763. This substantial reduction indicates that the EAFD effectively suppresses the resonant peak by enhancing energy dissipation and improving dynamic interaction between the

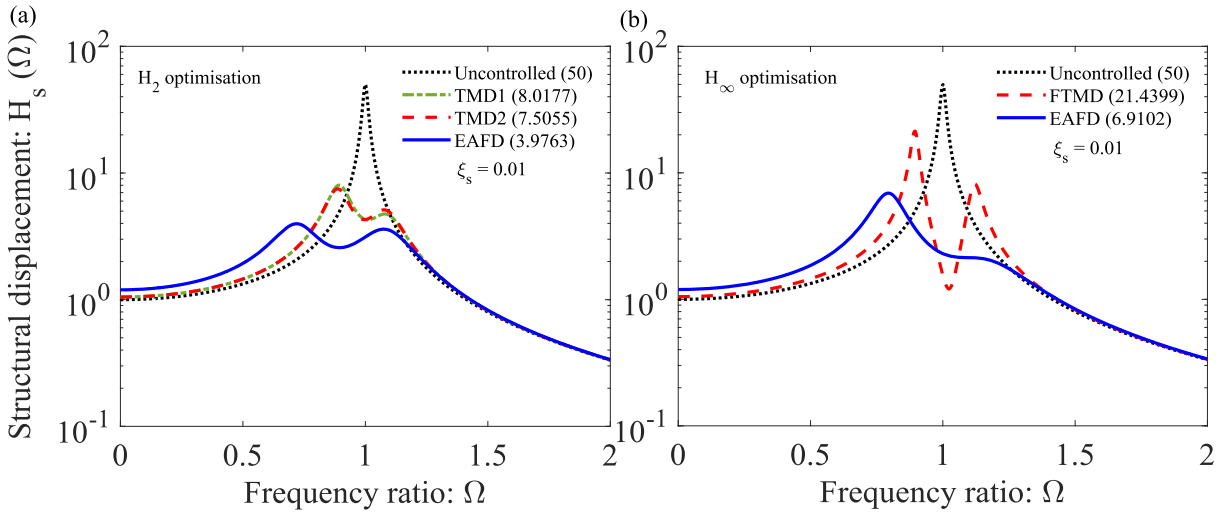

Fig. 6. The variations of structural displacements of the SDOF systems controlled by (a) H_2 and (b) H_∞ optimised dampers versus frequency ratio subjected to harmonic excitation.

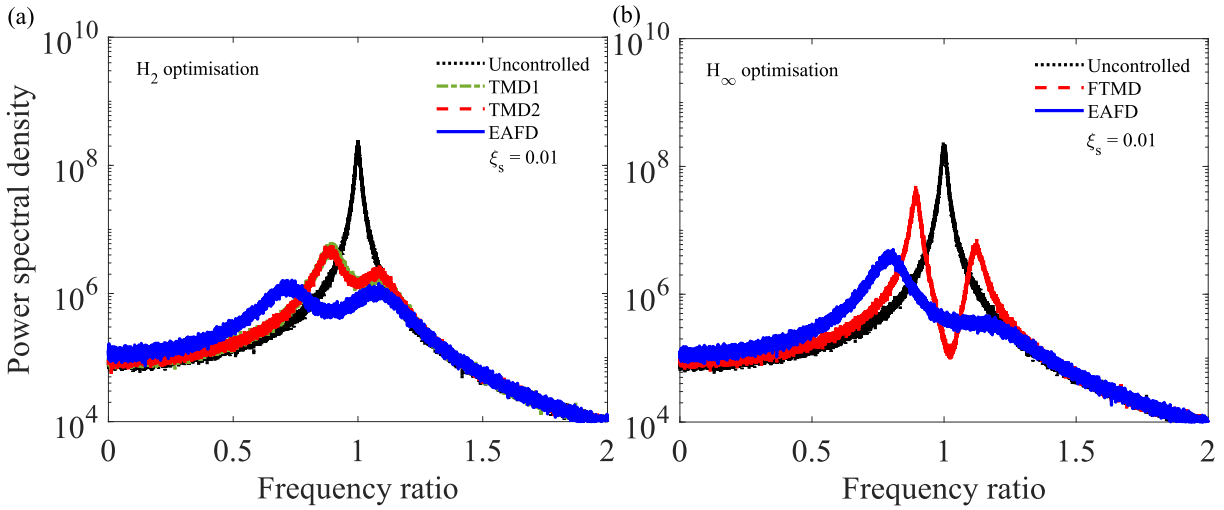

Fig. 7. The variations of structural displacements of the SDOF systems controlled by (a) H_2 and (b) H_∞ optimised dampers versus frequency ratio subjected to random white excitation.

damper and the primary structure. In particular, the combined effects of inertia amplification and magnetic stiffness modulation enable a broader and more efficient vibration attenuation compared to conventional TMDs. Accordingly, the EAFD achieves 50.40% and 47.02% greater dynamic response reduction than TMD1 and TMD2, respectively. Furthermore, the performance of H_∞ optimised dampers is examined, as shown in Fig. 6(b). The maximum displacement of the uncontrolled system remains 50, while the responses of the systems controlled by FTMD and EAFD are obtained as 21.4399 and 6.9102, respectively. The significantly lower response of the EAFD demonstrates its superior capability in limiting peak amplitudes under harmonic excitation. This improvement can be attributed to the synergistic interaction of nonlinear frictional damping and stiffness modulation, which enhances energy dissipation over a wider frequency range. As a result, the EAFD achieves 67.76% greater dynamic response reduction than the FTMD, highlighting its effectiveness in controlling vibrations under both resonant and off-resonant conditions. In addition to harmonic excitation, random white-noise excitation is applied at the base to evaluate the performance of the EAFD under broadband loading conditions. This analysis enables assessment of the damper effectiveness over a wide range of frequencies, which is essential for realistic structural excitations. Accordingly, the variations of structural displacements of the SDOF systems controlled by H_2 optimised dampers under random excitation are presented in Fig. 7(a).

Additionally, the displacement response of the uncontrolled structure is evaluated under random white-noise excitation, and the maximum response is obtained as 2.4983×10^8 dB/Hz. The SDOF systems controlled by TMD1 and TMD2 exhibit maximum displacement responses of 6.3321×10^6 dB/Hz and 5.721×10^6 dB/Hz, respectively, whereas the EAFD-controlled system shows a

Table 1
The details of the near field earthquake records.

Earthquake	Year	M_w	Recording station	Vs_{30}(m/s)	Component	E_s (km)	PGA,g
Irpinia, Italy-01	1980	6.9	Sturno	1000	MUL009	30.4	0.31
Superstition Hills-02	1987	6.5	Parachute Test Site	349	SUPERST	16.0	0.42
Loma Prieta	1989	6.9	LOMAP	371	HEC000	27.2	0.38
Erzican, Turkey	1992	6.7	Erzincan 11	275	ERZIKAN	9.0	0.49
Cape Mendocino	1992	7.0	CAPEMEND	713	NIS090	4.5	0.63
Landers	1992	7.3	Lucerne	685	LANDERS	44.0	0.79
Northridge-01	1994	6.7	Rinaldi Receiving Sta	282	NORTHR	10.9	0.87
Kocaeli, Turkey	1999	7.5	Izmit	811	KOCAELI	5.3	0.22
Chi-Chi, Taiwan	1999	7.6	TCU065	306	CHICHI	26.7	0.82
Chi-Chi, Taiwan	1999	7.6	TCU102	714	CHICHI	45.6	0.29
Duzce, Turkey	1999	7.1	Duzce	276	DUZCE	1.6	0.52

significantly lower response of 1.6186×10^6 dB/Hz. This substantial reduction indicates that the EAFD effectively suppresses broadband vibration energy by enhancing dissipation and improving dynamic interaction over a wide frequency range. Accordingly, the EAFD achieves 74.43% and 71.71% greater dynamic response reduction than TMD1 and TMD2, respectively. Furthermore, the dynamic response reduction capacity of H_∞ optimised dampers is evaluated, as shown in Fig. 7(b). The maximum displacement responses of the systems controlled by FTMD and EAFD are obtained as 4.956×10^7 dB/Hz and 5.0297×10^6 dB/Hz, respectively. The significantly lower response of the EAFD demonstrates its superior capability in attenuating broadband excitations. This improvement can be attributed to the combined effects of inertia amplification, magnetic stiffness modulation, and nonlinear frictional damping, which enhance energy dissipation across a wider frequency spectrum. As a result, the EAFD achieves 89.85% greater dynamic response reduction than the FTMD.

The consistent reduction in peak responses under both harmonic and random excitations demonstrates that the proposed EAFD provides not only resonance suppression but also effective broadband vibration control. Unlike conventional TMDs, whose performance is highly sensitive to tuning conditions, the combined effects of inertia amplification, magnetic stiffness modulation, and nonlinear damping enable the EAFD to maintain stable performance over a wide frequency range. This behaviour highlights the robustness of the proposed system and confirms its suitability for practical engineering applications subjected to uncertain and varying dynamic loads.

5.2. Time history result

In order to test the performed methodology across a wider range of real seismic excitation events, real earthquake ground motions are taken into consideration. Newmark-beta method is employed to perform this analysis. The mass of the main structure is 3000 tons, or $m_s = 3000$ tons. $T_s = 0.5$ s is the representation of the structure's stated time period of 0.5 s. The natural frequency of the structure is determined by its time period, which is expressed as $\omega_s = 2\pi/T_s$. It is assumed that the fundamental structure's viscous damping ratio is 0.01; this can be expressed as $\xi_s = 0.01$.

Table 1 lists the information of the near-field earthquake record with pulses. Buildings are more at risk from near-field earthquakes with pulses than from far-field ones. Therefore, near-field earthquake recordings with pulses that have a noticeable vertical component are used in the numerical analysis meant to evaluate each damper's vibration attenuation effectiveness. The damping factor is taken into consideration at 5%, and the near-field earthquake records with pulse spectra are displayed in Fig. 8.

The displacement responses of the primary structure controlled by the EAFD under the Irpinia, Italy-01 and Superstition Hills-02 earthquake excitations are evaluated and presented in Fig. 9(a) and (b), respectively. The results demonstrate that the EAFD effectively reduces both the peak and transient displacement responses compared to the uncontrolled and conventionally controlled systems. This improved performance can be attributed to the combined effects of inertia amplification, magnetic stiffness modulation, and nonlinear frictional damping, which enhance energy dissipation and stabilise the structural response under seismic excitations.

According to Fig. 9(a), the maximum displacement of the uncontrolled structure is obtained as 0.0049 m. The maximum displacement of the structure controlled by the TMD is reduced to 0.0026 m, while the EAFD-controlled system exhibits a further reduction to 0.0019 m. This significant decrease indicates that the EAFD more effectively suppresses both peak and transient responses under seismic excitation. In particular, the enhanced performance can be attributed to the combined effects of inertia amplification, magnetic stiffness modulation, and nonlinear frictional damping, which improve energy dissipation and dynamic stability. Consequently, the EAFD achieves a 26.92% higher vibration reduction capability compared to the conventional TMD. According to Fig. 9(b), the peak displacement of the uncontrolled structure is observed to be 0.0082 m. The implementation of a conventional TMD reduces this value to 0.0055 m, whereas the EAFD further decreases the maximum displacement to 0.0038 m. This pronounced reduction demonstrates that the EAFD is more effective in mitigating both peak and transient structural responses under seismic excitation. The improved performance is primarily attributed to the synergistic interaction of inertia amplification, magnetic stiffness modulation, and nonlinear frictional damping, which collectively enhance energy dissipation and dynamic stability. As a result, the EAFD provides approximately 30.90% greater vibration reduction compared to the conventional TMD. Similarly, the displacement responses for other considered earthquake records are presented in Table 2 and are further evaluated to assess the performance of the proposed damper.

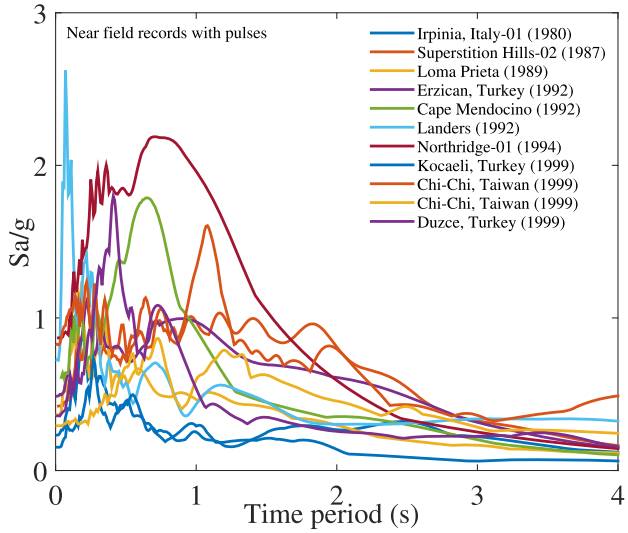

Fig. 8. The response spectra of the earthquake records.

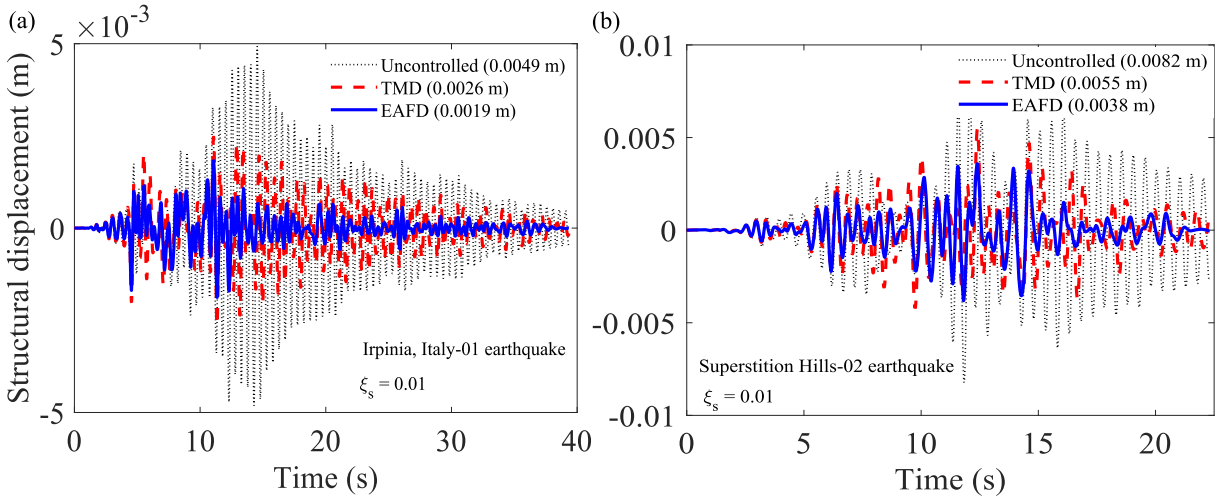

Fig. 9. The variations of structural displacements of the SDOF systems controlled by dampers versus time subjected to (a) Irpinia, Italy-01 and (b) Superstition Hills-02 earthquakes.

Table 2
The maximum displacements of the uncontrolled and controlled structures. The displacement reduction capacity is derived by comparing the maximum displacement of SDOF system controlled by TMD and EAFD.

Earthquake	u_s^{max} (m)			Displacement reduction capacity (%)
	Uncontrolled	TMD	EAFD	EAFD
Irpinia, Italy-01	0.0049	0.0026	0.0019	26.92307692
Superstition Hills-02	0.0082	0.0055	0.0038	30.90909091
Loma Prieta	0.0055	0.004	0.0034	15
Erzican, Turkey	0.0066	0.0064	0.0042	34.375
Cape Mendocino	0.0117	0.0082	0.0077	6.097560976
Landers	0.0041	0.0035	0.0024	31.42857143
Northridge-01	0.0072	0.0056	0.0047	16.07142857
Kocaeli, Turkey	0.0044	0.0039	0.0017	56.41025641
Chi-Chi, Taiwan	0.0088	0.0069	0.0052	24.63768116
Chi-Chi, Taiwan	0.0063	0.0051	0.0044	13.7254902
Duzce, Turkey	0.011	0.0072	0.0066	8.333333333
Average	0.007154545	0.005354545	0.004181818	23.99195363

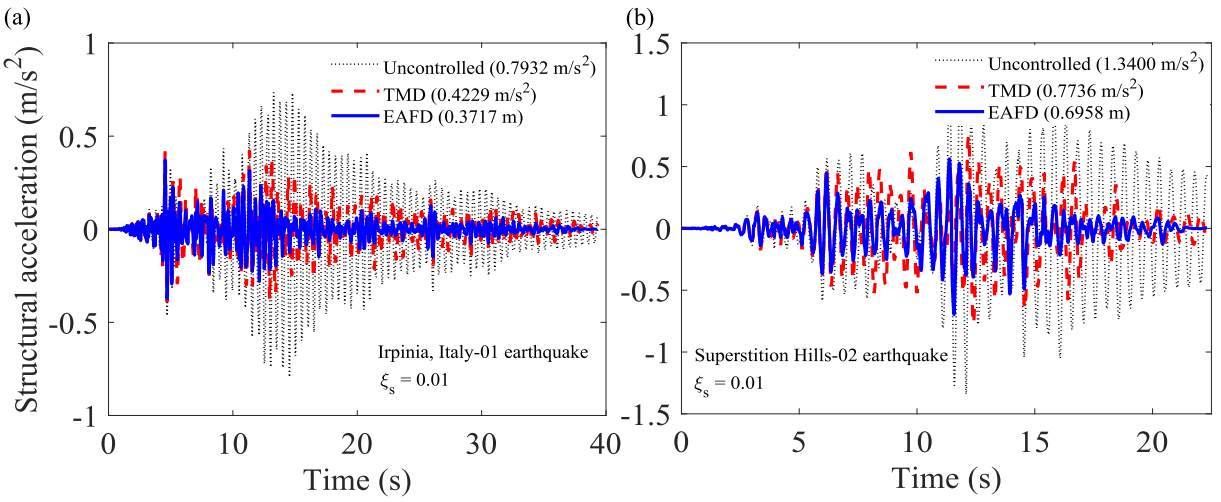

Fig. 10. The variations of structural accelerations of the SDOF systems controlled by dampers versus time subjected to (a) Irpinia, Italy-01 and (b) Superstition Hills-02 earthquakes.

Table 3
The maximum accelerations of the uncontrolled and controlled structures. The acceleration reduction capacity is derived by comparing the maximum acceleration of SDOF system controlled by TMD and EAFD.

Earthquake	$\ddot{u}_s^{\max}$ (m/s^2)			Acceleration reduction capacity (%)
	Uncontrolled	TMD	EAFD	EAFD
Irpinia, Italy-01	0.7932	0.4229	0.3717	12.10688106
Superstition Hills-02	1.34	0.7736	0.6958	10.05687694
Loma Prieta	0.8531	0.7244	0.5803	19.89232468
Erzican, Turkey	0.9524	0.7843	0.7216	7.994389902
Cape Mendocino	1.9069	0.9419	0.7844	16.72152033
Landers	1.2678	1.0256	0.8864	13.5725429
Northridge-01	1.4202	1.0797	0.9115	15.57840141
Kocaeli, Turkey	0.7072	0.6311	0.3607	42.84582475
Chi-Chi, Taiwan	1.3977	0.8792	0.6022	31.50591447
Chi-Chi, Taiwan	0.8644	0.5646	0.3923	30.5171803
Duzce, Turkey	1.8135	1.0309	0.9053	12.18352896
Average	1.210581818	0.805290909	0.655654545	19.3613987

The displacement response reduction capability of the EAFD is evaluated by comparing the average maximum displacement amplitudes of structures controlled by the conventional and EAFD systems, as presented in Table 2. The results indicate that the EAFD achieves a 23.99% greater displacement reduction capacity than the conventional damper. Fig. 10(a) and (b) present the acceleration responses of the primary structure controlled by the EAFD under the Irpinia, Italy-01 and Superstition Hills-02 earthquake excitations, respectively.

According to Fig. 10(a), the maximum acceleration of the uncontrolled structure is obtained as 0.7932 m/s^2. The maximum acceleration of the TMD-controlled structure is reduced to 0.4229 m/s^2, while the EAFD-controlled structure exhibits a further reduction to 0.3717 m/s^2. This reduction indicates that the EAFD effectively limits acceleration peaks, which is critical for improving structural safety and serviceability under seismic loading. The improved performance can be attributed to the combined effects of inertia amplification, magnetic stiffness modulation, and nonlinear frictional damping, which enhance energy dissipation and reduce high-frequency response components. Consequently, the EAFD achieves a 12.10% higher acceleration reduction capability compared to the conventional TMD. According to Fig. 10(b), the peak acceleration of the uncontrolled structure is recorded as 1.3400 m/s^2. The introduction of a conventional TMD reduces this value to 0.7736 m/s^2, while the EAFD further lowers the maximum acceleration to 0.6958 m/s^2. This reduction demonstrates the capability of the EAFD to more effectively limit acceleration peaks, which is essential for enhancing structural safety and serviceability under seismic excitation. The superior performance is attributed to the combined influence of inertia amplification, magnetic stiffness modulation, and nonlinear frictional damping, which collectively improve energy dissipation and attenuate high-frequency response components. Consequently, the EAFD provides approximately 10.05% greater acceleration reduction compared to the conventional TMD. The acceleration response reduction capability of the EAFD is evaluated by comparing the average maximum acceleration amplitudes of structures controlled by the conventional and EAFD systems, as presented in Table 3.

The results indicate that the EAFD achieves a 19.36% greater acceleration reduction capacity compared to the conventional damper.

6. Summary and conclusions

An advanced elastomagnetic amplifier and an elastomagnetic amplifier friction damper are introduced. These novel amplifiers and dampers circumvent the limited frequency bandwidth and limited adaptability of traditional tuned mass dampers by combining stiffness and mass amplification techniques. The exact closed-form expressions for the optimal design parameters of the damper are derived using the H_2 and H_∞ optimisation techniques. Using the transfer matrix, the frequency domain responses under harmonic and random noise excitations showed notable gains in vibration mitigation capabilities. Their efficiency in reducing structural responses is further demonstrated through comparative studies using near-field earthquake records and the Newmark-beta method. With increases of up to 23.99% under seismic excitations, the suggested designs continuously beat traditional TMDs in terms of vibration reduction capability.

- The integration of magnetic stiffness amplification elements for extended frequency control is one of the research's primary accomplishments.
- Improved dissipation of energy using frictional damping systems and magnets.
- Sturdy operation in a variety of dynamic circumstances, including seismic applications.

These results demonstrate that the novel damper provides effective and flexible vibration control for buildings exposed to broadband and erratic excitations, offering a viable solution to contemporary engineering challenges. One of the main contributions of this work is the introduction of elastomagnetic amplifiers and elastomagnetic amplifier friction dampers, which enable the simultaneous enhancement of effective mass, stiffness, and damping characteristics within a unified framework. In addition, new closed-form expressions for the optimal design parameters of the proposed dampers are derived, providing direct analytical insight into system behaviour and facilitating efficient and reliable design implementation. To further enhance their applicability, future research may explore extensions to multi-degree-of-freedom systems.

CRediT authorship contribution statement

Sudip Chowdhury: Writing – review & editing, Writing – original draft, Visualization, Validation, Supervision, Software, Resources, Project administration, Methodology, Investigation, Funding acquisition, Formal analysis, Data curation, Conceptualization; **Sondipon Adhikari:** Writing – review & editing, Visualization, Supervision, Software, Resources, Methodology, Conceptualization.

Data availability

No data was used for the research described in the article.

Declaration of competing interest

The authors declare that they have no known competing financial interests or personal relationships that could have appeared to influence the work reported in this paper.

Acknowledgements

The authors would like to acknowledge the Post Doctoral grant received from The University of Glasgow during the period of this research work.

Appendix A. The closed-form expressions from H_2 optimisation

The closed-form expression from Eq. (34) is listed below.

$$
\begin{aligned}
N_1 = {} & 16\left(\begin{array}{c}\kappa^2\omega_d^4\left(\mu_d+1\right)^4(\nu-1)^2\left(\cot^4(\phi)\right)\\ +2\kappa\left(\left(\mu_d+1\right)^2(\nu-1)\omega_d^2-\frac{\omega_s^2\left(\mu_d-2\right)}{2}\right)\omega_d^2\left(\mu_d+1\right)^2(\nu-1)\left(\cot^2(\phi)\right)\\ +\left(\mu_d+1\right)^4(\nu-1)^2\omega_d^4+\omega_s^4\\ -\left(\left(-4\xi_d^2+\nu-1\right)\mu_d-4\xi_d^2-2\nu+2\right)\left(\mu_d+1\right)^2\omega_s^2\omega_d^2\end{array}\right)\left(\sin^6(\phi)\right)\\
& +32\left(\begin{array}{c}\kappa^2\mu_d\omega_d^4\left(\mu_d+1\right)^3(\nu-1)^2\left(\cot^4(\phi)\right)\\ +2\kappa\,\omega_d^2\left(\mu_d+1\right)\left(\begin{array}{c}\mu_d\left(\mu_d+1\right)^2(\nu-1)\omega_d^2\\ -\frac{\omega_s^2\left(\mu_d^2-\mu_d-\frac{1}{2}\right)}{2}\end{array}\right)(\nu-1)\left(\cot^2(\phi)\right)\\ +\mu_d\left(\mu_d+1\right)^3(\nu-1)^2\omega_d^4+\frac{\omega_s^4}{2}\\ -\left(\left(-5\xi_d^2+\nu-1\right)\mu_d^2+\left(-7\xi_d^2-\nu+1\right)\mu_d-2\xi_d^2-\frac{\nu}{2}+\frac{1}{2}\right)\left(\mu_d+1\right)\omega_s^2\omega_d^2\end{array}\right)\mu_a\left(\sin^4(\phi)\right)\\
& +24\left(\begin{array}{c}\kappa^2\mu_d^2\omega_d^4\left(\mu_d+1\right)^2(\nu-1)^2\left(\cot^4(\phi)\right)\\ +2\kappa\left(\mu_d\left(\mu_d+1\right)^2(\nu-1)\omega_d^2-\frac{\left(\mu_d^2-\frac{1}{2}\right)\omega_s^2}{2}\right)\omega_d^2\mu_d(\nu-1)\left(\cot^2(\phi)\right)\\ +\mu_d^2\left(\mu_d+1\right)^2(\nu-1)^2\omega_d^4+\frac{\omega_s^4}{6}\\ -\left(\left(-\frac{20\xi_d^2}{3}+\nu-1\right)\mu_d^3-12\mu_d^2\xi_d^2+\left(-6\xi_d^2-\frac{\nu}{2}+\frac{1}{2}\right)\mu_d-\frac{2\xi_d^2}{3}\right)\omega_s^2\omega_d^2\end{array}\right)\mu_a^2\left(\sin^2(\phi)\right)\\
& +\omega_d^2\mu_d\mu_a^3\left(\begin{array}{c}8\kappa^2\mu_d^2\omega_d^2(\nu-1)^2\left(\mu_d+1\right)\left(\cot^4(\phi)\right)\\ +\kappa\,\mu_d^2(\nu-1)\left(\begin{array}{c}\kappa\mu_a\mu_d\omega_d^2(\nu-1)\left(\cot^2(\phi)\right)\\ +16\left(\mu_d+1\right)(\nu-1)\omega_d^2-8\omega_s^2\end{array}\right)\left(\cot^2(\phi)\right)\\ +2\kappa\,\mu_d^2\mu_a\left(\mu_d(\nu-1)\omega_d^2-\frac{\omega_s^2}{2}\right)(\nu-1)\left(\cot^2(\phi)\right)+2\left(\csc^4(\phi)\right)\mu_a^2\mu_d^2\xi_d^2\omega_s^2\\ +\left(\mu_d^2(\nu-1)^2\omega_d^2-\left(\left(-20\xi_d^2+\nu-1\right)\mu_d-12\xi_d^2\right)\omega_s^2\right)\mu_d\mu_a\left(\csc^2(\phi)\right)\\ +8\mu_d^2(\nu-1)^2\left(\mu_d+1\right)\omega_d^2-8\left(\left(-10\xi_d^2+\nu-1\right)\mu_d^2-12\mu_d\xi_d^2-3\xi_d^2\right)\omega_s^2\end{array}\right)
\end{aligned}
\tag{A.1}
$$

The closed-form expression from Eq. (38) is listed below.

$$
\begin{aligned}
N_2 = {} & 16\left(\begin{array}{c}\kappa^2\omega_d^4\left(1+\mu_d\right)^4(\nu-1)^2\left(\cot^4(\phi)\right)\\ +2\omega_d^2\left(\left(1+\mu_d\right)^2(\nu-1)\omega_d^2-\frac{\omega_s^2\left(\mu_d-2\right)}{2}\right)\kappa(\nu-1)\left(1+\mu_d\right)^2\left(\cot^2(\phi)\right)\\ +\left(1+\mu_d\right)^4(\nu-1)^2\omega_d^4-\omega_s^2\left(\mu_d-2\right)\left(1+\mu_d\right)^2(\nu-1)\omega_d^2+\omega_s^4\end{array}\right)\left(\sin^6(\phi)\right)\\
& +32\mu_a\left(\begin{array}{c}\kappa^2\mu_d\omega_d^4\left(1+\mu_d\right)^3(\nu-1)^2\left(\cot^4(\phi)\right)\\ +\left(\begin{array}{c}\mu_d\left(1+\mu_d\right)^2(\nu-1)\omega_d^2-\frac{\omega_s^2\left(\mu_d^2-\mu_d-\frac{1}{2}\right)}{2}\end{array}\right)\\ 2\omega_d^2\kappa(\nu-1)\left(1+\mu_d\right)\left(\cot^2(\phi)\right)\\ +\mu_d\left(1+\mu_d\right)^3(\nu-1)^2\omega_d^4+\frac{\omega_s^4}{2}\\ -\omega_s^2\left(\mu_d^2-\mu_d-\frac{1}{2}\right)(\nu-1)\left(1+\mu_d\right)\omega_d^2\end{array}\right)\left(\sin^4(\phi)\right)\\
& +24\left(\begin{array}{c}\kappa^2\mu_d^2\omega_d^4\left(1+\mu_d\right)^2(\nu-1)^2\left(\cot^4(\phi)\right)\\ +2\omega_d^2\left(\mu_d\left(1+\mu_d\right)^2(\nu-1)\omega_d^2-\frac{\omega_s^2\left(\mu_d^2-\frac{1}{2}\right)}{2}\right)\kappa(\nu-1)\mu_d\left(\cot^2(\phi)\right)\\ +\mu_d^2\left(1+\mu_d\right)^2(\nu-1)^2\omega_d^4-\omega_s^2\left(\mu_d^2-\frac{1}{2}\right)(\nu-1)\mu_d\omega_d^2+\frac{\omega_s^4}{6}\end{array}\right)\mu_a^2\left(\sin^2(\phi)\right)\\
& +\left(\begin{array}{c}8\kappa^2\omega_d^2\left(1+\mu_d\right)(\nu-1)\left(\cot^4(\phi)\right)\\ +\left(\begin{array}{c}\kappa\mu_a\mu_d\omega_d^2(\nu-1)\left(\cot^2(\phi)\right)\\ +16\left(1+\mu_d\right)(\nu-1)\omega_d^2-8\omega_s^2\end{array}\right)\kappa\left(\cot^2(\phi)\right)\\ +2\left(\mu_d(\nu-1)\omega_d^2-\frac{\omega_s^2}{2}\right)\mu_a\kappa\left(\cot^2(\phi)\right)\\ +\mu_a\left(\mu_d(\nu-1)\omega_d^2-\omega_s^2\right)\left(\csc^2(\phi)\right)\\ +8\left(1+\mu_d\right)(\nu-1)\omega_d^2-8\omega_s^2\end{array}\right)\omega_d^2\mu_a^3(\nu-1)\mu_d^3
\end{aligned}
\tag{A.2}
$$

Appendix B. The closed-form expressions from H_∞ optimisation

The closed-form expressions from Eq. (56) are listed below.

$$Z_1 = -2\Big(\big(\csc^2(\phi)\big)\mu_a\mu_d\Omega_{1,2}^2 + 2\mu_d\Omega_{1,2}^2 + 2\Omega_{1,2}^2 - 2\Big)\Omega_{1,2}^4\big(2\big(\sin^2(\phi)\big)+\mu_a\big)^4 \Omega_d^4\big(\big(2\mu_d+2\big)\big(\sin^2(\phi)\big)+\mu_a\mu_d\big)^3\big(\csc^{14}(\phi)\big) \tag{B.1}$$

$$Z_2 = \begin{bmatrix} \Big(-4\Omega_d^2\big(\big(2\mu_d+2\big)\big(\sin^2(\phi)\big)+\mu_a\mu_d\big)^2\big(\csc^{12}(\phi)\big)\big(2\big(\sin^2(\phi)\big)+\mu_a\big)^4\Big)\Omega_{1,2}^8 \\ +\begin{bmatrix} -8\begin{pmatrix} \begin{pmatrix} 2\kappa\,\Omega_d^2\big(\mu_d+1\big)(\nu-1)\big(\cot^2(\phi)\big) \\ -1+2\big(\mu_d+1\big)(\nu-1)\Omega_d^2 \end{pmatrix}\big(\sin^2(\phi)\big) \\ +\mu_a\Big(\kappa\mu_d\Omega_d^2(\nu-1)\big(\cot^2(\phi)\big)-\frac{1}{2}+\mu_d(\nu-1)\Omega_d^2\Big) \end{pmatrix} \\ \Omega_d^2\big(\csc^{12}(\phi)\big)\big(\big(2\mu_d+2\big)\big(\sin^2(\phi)\big)+\mu_a\mu_d\big)^2\big(2\big(\sin^2(\phi)\big)+\mu_a\big)^3 \end{bmatrix}\Omega_{1,2}^6 \\ +G_1\Omega_{1,2}^4 + G_2 \end{bmatrix} \tag{B.2}$$

$$G_1 = -4\begin{bmatrix} \begin{pmatrix} \frac{1}{4}+\mu_d^2(\nu-1)^2\Omega_d^4-\frac{(\nu-1)\mu_d\Omega_d^2}{2} \end{pmatrix}\mu_a^4\mu_d^2\big(\csc^{12}(\phi)\big) \\ +2\mu_a^3\mu_d\begin{pmatrix} \mu_a\mu_d^2\Big(-\frac{1}{4}+(\nu-1)\mu_d\Omega_d^2\Big)\kappa\,\Omega_d^2(\nu-1)\big(\cot^2(\phi)\big) \\ +4\mu_d^2(\nu-1)^2\big(\mu_d+1\big)\Omega_d^4+\frac{1}{2} \\ -2\mu_d\Big(\mu_d+\frac{3}{2}\Big)(\nu-1)\Omega_d^2+\mu_d \end{pmatrix}\big(\csc^{10}(\phi)\big) \\ +\mu_a^2\mu_d\begin{pmatrix} \kappa^2\mu_a^2\mu_d^3\Omega_d^4(\nu-1)^2\big(\cot^4(\phi)\big) \\ +16\mu_a\mu_d\Big(\mu_d\big(\mu_d+1\big)(\nu-1)\Omega_d^2-\frac{\mu_d}{4}-\frac{3}{8}\Big) \\ \kappa\,\Omega_d^2(\nu-1)\big(\cot^2(\phi)\big) \\ +24\mu_d\big(\mu_d+1\big)^2(\nu-1)^2\Omega_d^4+6 \\ -12\Big(\mu_d^2+3\mu_d+\frac{3}{2}\Big)(\nu-1)\Omega_d^2+6\mu_d \end{pmatrix}\big(\csc^8(\phi)\big) \\ +8\mu_a\begin{pmatrix} \kappa^2\mu_a^2\mu_d^3\Omega_d^4(\nu-1)^2\big(\mu_d+1\big)\big(\cot^4(\phi)\big) \\ +6\mu_a\mu_d\kappa\,\Omega_d^2\Big(\mu_d\big(\mu_d+1\big)^2(\nu-1)\Omega_d^2-\frac{\mu_d^2}{4}-\frac{3\mu_d}{4}-\frac{3}{8}\Big) \\ (\nu-1)\big(\cot^2(\phi)\big) \\ +4\mu_d\big(\mu_d+1\big)^3(\nu-1)^2\Omega_d^4+\frac{3\mu_d}{2}+\mu_d^2 \\ -2\Big(\mu_d^2+\frac{7}{2}\mu_d+1\Big)(\nu-1)\big(\mu_d+1\big)\Omega_d^2 \end{pmatrix}\big(\csc^6(\phi)\big) \\ +4\begin{pmatrix} 6\kappa^2\mu_a^2\mu_d^2\Omega_d^4\big(\mu_d+1\big)^2(\nu-1)^2\big(\cot^4(\phi)\big) \\ +16\mu_a\kappa\,\Omega_d^2\Big(\mu_d\big(\mu_d+1\big)^2(\nu-1)\Omega_d^2-\frac{\mu_d^2}{4}-\frac{7\mu_d}{8}-\frac{1}{4}\Big) \\ (\nu-1)\big(\mu_d+1\big)\big(\cot^2(\phi)\big) \\ +4\big(\mu_d+1\big)^4(\nu-1)^2\Omega_d^4-2\big(\mu_d+4\big)\big(\mu_d+1\big)^2(\nu-1)\Omega_d^2 \\ +\mu_d^2+2\mu_d \end{pmatrix}\big(\csc^4(\phi)\big) \\ +32\begin{pmatrix} \kappa\mu_a\mu_d\Omega_d^2\big(\mu_d+1\big)(\nu-1)\big(\cot^2(\phi)\big) \\ +\big(\mu_d+1\big)^2(\nu-1)\Omega_d^2-\frac{\mu_d}{4}-1 \end{pmatrix} \\ \big(\cot^2(\phi)\big)\kappa\,\Omega_d^2(\nu-1)\big(\mu_d+1\big)^2\big(\csc^2(\phi)\big) \\ +16\kappa^2\Omega_d^4\big(\cot^4(\phi)\big)\big(\mu_d+1\big)^4(\nu-1)^2 \\ \Omega_d^2\big(2\big(\sin^2(\phi)\big)+\mu_a\big)^2 \end{bmatrix} \tag{B.3}$$

$$G_2 = 8\big(\big(2\mu_d+2\big)\big(\sin^2(\phi)\big)+\mu_a\mu_d\big)^3\big(\big(\cot^2(\phi)\big)\kappa+1\big)^2 \Omega_d^6\big(2\big(\sin^2(\phi)\big)+\mu_a\big)^2\big(\csc^{10}(\phi)\big)(\nu-1)^2 \tag{B.4}$$

$$
Z_3 = \left(\begin{array}{c}
\left(\begin{array}{c}
\kappa^2 \Omega_d^4 \left(\mu_d+1\right)^2 (\nu-1)^2 \left(\cot^4(\phi)\right) \\
+2(\nu-1)\left(\begin{array}{c} \left(\mu_d+1\right)^2 (\nu-1)\Omega_d^2 \\ +\left(\Omega_{1,2}^2-\frac{1}{2}\right)\mu_d+\Omega_{1,2}^2 \end{array} \right)\Omega_d^2 \kappa\left(\cot^2(\phi)\right) \\
+\left(\mu_d+1\right)^2 (\nu-1)^2 \Omega_d^4 + 2\left(\left(\Omega_{1,2}^2-\frac{1}{2}\right)\mu_d+\Omega_{1,2}^2\right)(\nu-1)\Omega_d^2+\Omega_{1,2}^4
\end{array} \right)\left(\sin^4(\phi)\right) \\
+\mu_a \left(\begin{array}{c}
\kappa^2 \mu_d \Omega_d^4 (\nu-1)^2 \left(\mu_d+1\right)\left(\cot^4(\phi)\right) \\
+2(\nu-1)\Omega_d^2 \left(\begin{array}{c} \mu_d\left(\mu_d+1\right)(\nu-1)\Omega_d^2 \\ +\left(\Omega_{1,2}^2-\frac{1}{2}\right)\mu_d+\frac{\Omega_{1,2}^2}{2} \end{array} \right)\kappa\left(\cot^2(\phi)\right) \\
+\mu_d(\nu-1)^2\left(\mu_d+1\right)\Omega_d^4+\Omega_{1,2}^4 \\
+2\left(\left(\Omega_{1,2}^2-\frac{1}{2}\right)\mu_d+\frac{\Omega_{1,2}^2}{2}\right)(\nu-1)\Omega_d^2
\end{array} \right)\left(\sin^2(\phi)\right) \\
+\frac{\mu_a^2 \left(\begin{array}{c}
\kappa^2 \mu_d^2 \Omega_d^4 (\nu-1)^2 \left(\cot^4(\phi)\right) \\
+2\mu_d(\nu-1)\Omega_d^2\left(\mu_d(\nu-1)\Omega_d^2+\Omega_{1,2}^2-\frac{1}{2}\right)\kappa\left(\cot^2(\phi)\right) \\
+\mu_d^2(\nu-1)^2\Omega_d^4+2\left(\Omega_{1,2}^2-\frac{1}{2}\right)\mu_d(\nu-1)\Omega_d^2+\Omega_{1,2}^4
\end{array} \right)}{4}
\end{array} \right)
$$

$$
+\left(\csc^8(\phi)\right)\left(\begin{array}{c}
\left(\kappa\Omega_d^2\left(\mu_d+1\right)(\nu-1)\left(\cot^2(\phi)\right)+\left(\mu_d+1\right)(\nu-1)\Omega_d^2+\Omega_{1,2}^2\right)\left(\sin^2(\phi)\right) \\
+\frac{\mu_a\left(\kappa\mu_d\Omega_d^2(\nu-1)\left(\cot^2(\phi)\right)+\mu_d(\nu-1)\Omega_d^2+\Omega_{1,2}^2\right)}{2}
\end{array} \right)
$$

$$
-32\left(\begin{array}{c}
\left(\begin{array}{c}
\kappa\Omega_d^2(\nu-1)\left(\mu_d\Omega_{1,2}^2+\Omega_{1,2}^2-1\right)\left(\cot^2(\phi)\right) \\
+(\nu-1)\left(\mu_d\Omega_{1,2}^2+\Omega_{1,2}^2-1\right)\Omega_d^2+\Omega_{1,2}^4-\Omega_{1,2}^2
\end{array} \right)\left(\sin^2(\phi)\right) \\
+\frac{\Omega_{1,2}^2\mu_a\left(\kappa\mu_d\Omega_d^2(\nu-1)\left(\cot^2(\phi)\right)+\mu_d(\nu-1)\Omega_d^2+\Omega_{1,2}^2-1\right)}{2}
\end{array} \right) \tag{B.5}
$$

References

[1] X. Ma, R. Yu, H. Li, J. Jing, Z. Zhang, Vibration mitigation in a spline-shafting system via an auxiliary support: simulation and experiment, Mech. Syst. Signal Process. 224 (2025) 112120.

[2] J.-M. Shin, H.-J. Ahn, Vibration issues in precision equipment: challenges and mitigation strategies of pneumatic vibration isolators, Int. J. Precis. Eng. Manuf. 26 (9) (2025) 2223–2242.

[3] A. Zar, Z. Hussain, M. Akbar, T. Rabczuk, Z. Lin, S. Li, B. Ahmed, Towards vibration-based damage detection of civil engineering structures: overview, challenges, and future prospects, Int. J. Mech. Mater. Des. 20 (3) (2024) 591–662.

[4] T. Zhang, W. Wang, X. Li, B. Wang, Vibration mitigation in offshore wind turbine under combined wind-wave-earthquake loads using the tuned mass damper inerter, Renew. Energy 216 (2023) 119050.

[5] S. Zhang, J. Zhou, H. Ding, K. Wang, Micro-vibration mitigation of a Cantilever beam by one-third power nonlinear energy sinks, Aerosp. Sci. Technol. 153 (2024) 109409.

[6] J. Tang, K. Dai, Y. Luo, M.A. Bezabeh, Z. Ding, Integrated control strategy for the vibration mitigation of wind turbines based on pitch angle control and TMDI systems, Eng. Struct. 303 (2024) 117529.

[7] T. Konar, A.D. Ghosh, Tuned mass damper inerter for seismic control of multi-story buildings: ten years since inception, in: Structures, 63, Elsevier, 2024, p. 106459.

[8] L. Wang, S. Nagarajaiah, Y. Zhou, W. Shi, Experimental study on adaptive-passive tuned mass damper with variable stiffness for vertical human-induced vibration control, Eng. Struct. 280 (2023) 115714.

[9] D. McNamara, A. Pandit, A. Malekjafarian, Optimized design of multiple tuned mass dampers for vibration control of offshore wind turbines, Ocean Eng. 305 (2024) 117912.

[10] H.Q. Cao, Combined tuned mass dampers for structural vibration control, Int. J. Non-Linear Mech. 157 (2023) 104550.

[11] P.R. Marrazzo, R. Montuori, E. Nastri, G. Benzoni, Advanced seismic retrofitting with high-mass-ratio tuned mass dampers, Soil Dyn. Earthq. Eng. 179 (2024) 108544.

[12] L. Wang, Y. Zhou, S. Nagarajaiah, W. Shi, Bi-directional semi-active tuned mass damper for torsional asymmetric structural seismic response control, Eng. Struct. 294 (2023) 116744.

[13] Z. Lu, S. Zhao, C. Ma, K. Dai, Experimental and analytical study on the performance of wind turbine tower attached with particle tuned mass damper, Eng. Struct. 294 (2023) 116784.

[14] N.-A. Tran, H.-L. Bui, Rolling tuned mass damper for vibration control of building structures subjected to earthquakes: a comparative study, Soil Dyn. Earthq. Eng. 194 (2025) 109376.

[15] L. Wang, Y. Zhou, W. Shi, Seismic response control of a nonlinear tall building under mainshock–aftershock sequences using semi-active tuned mass damper, Int. J. Struct. Stab. Dyn. 23 (16n18) (2023) 2340027.

[16] J. Zhang, F. Xie, Z. Ma, X.-J. Liu, H. Zhao, Design of parallel multiple tuned mass dampers for the vibration suppression of a parallel machining robot, Mech. Syst. Signal Process. 200 (2023) 110506.

[17] Y. Gao, E. Zhai, S. Li, Z. Zhang, Z. Xu, G. Zhang, V. Racic, J. Chen, L. Wang, Z. Zhang, Integrated design and real-world application of a tuned mass damper (TMD) with displacement constraints for large offshore monopile wind turbines, Ocean Eng. 292 (2024) 116568.

[18] O.K. Soureshjani, S.H.H. Lavassani, Performance of tuned particle impact damper and tuned mass damper seismic control systems considering mainshock-aftershock, in: Structures, 56, Elsevier, 2023, p. 104924.

[19] N.-A. Tran, V.-B. Hoang, H.-L. Bui, H.Q. Cao, Upgraded double tuned mass dampers for vibration control of structures under earthquakes, Comput. Struct. 310 (2025) 107700.

[20] M. Roozbahan, G. Turan, An improved passive tuned mass damper assisted by dual stiffness, in: Structures, 50, Elsevier, 2023, pp. 1598–1607.

[21] H. Zhang, B. Wen, X. Tian, X. Li, Y. Dong, M. Wang, Z. Peng, Experimental study on mitigating vibration of floating offshore wind turbine using tuned mass damper, Ocean Eng. 288 (2023) 115974.

[22] M.A. Shahraki, R. Kamgar, H. Heidarzadeh, Damage-based design of multiple tuned mass dampers to improve the seismic performance of steel frame structures, Soil Dyn. Earthq. Eng. 173 (2023) 108062.

[23] S. Djerouni, R. Garcia, Seismic behavior of buildings with tuned mass friction dampers optimized with a novel PSO-GWO hybrid algorithm, Soil Dyn. Earthq. Eng. 200 (2026) 109739.
[24] G.-L. Lin, C.-C. Lin, T.-H. Yang, H.-Y. Lung, Experimental verification of seismic vibration control of high-rise buildings with friction-type multiple tuned mass dampers, Eng. Struct. 302 (2024) 117401.
[25] B. Besharatian, H.T. Riahi, R. Garcia, I. Hajirasouliha, A practical optimisation method for friction tuned mass dampers in multi-storey buildings subjected to earthquake excitations, Soil Dyn. Earthq. Eng. 184 (2024) 108857.
[26] A.R. Özuygur, S. Elias, Seismic fragility assessment of structures with friction pendulum isolators, tuned mass dampers, and hybrid control systems, in: Structures, 82, Elsevier, 2025, p. 110545.
[27] M. Zhang, H. Lu, F. Xu, M. Wang, A novel tuned mass damper with negative stiffness mechanism for low-frequency vertical vibration control, J. Struct. Eng. 152 (5) (2026) 04026051.
[28] K. Ye, Y. Wang, L. Hu, Optimized negative stiffness friction isolator–tuned viscous mass damper system for base-isolated buildings, J. Struct. Eng. 152 (2) (2026) 04025273.
[29] T. Sun, L. Peng, X. Ji, X. Li, Development of a negative stiffness friction damping device with an amplification mechanism, Eng. Struct. 275 (2023) 115286.
[30] R. Zhang, J. Huang, Hybrid analytical optimal approach and comparative analyses for tuned viscous mass damper with negative stiffness (TVMDNS), J. Vib. Eng. Technol. 12 (5) (2024) 7175–7192.
[31] Q. Lyu, Z. Zhang, B. Fu, J. Ye, L. Liu, Seismic mitigation mechanism and optimal parameter analysis of tuned negative stiffness amplifying damper (TNSAD) for base-isolated structures, J. Build. Eng. 111 (2025) 113568.
[32] P. Chen, B. Wang, K. Ma, Optimal design and numerical studies of negative stiffness device–TMD controlled systems using PSO algorithm, Soil Dyn. Earthq. Eng. 189 (2025) 109111.
[33] B. Besharatian, H.T. Riahi, R. Garcia, I. Hajirasouliha, Particle swarm optimization of friction tuned mass dampers subjected to ground motion records, Soil Dyn. Earthq. Eng. 172 (2023) 107995.
[34] S.F. Labbafi, A. Shooshtari, E. Mohtashami, Optimal design of friction tuned mass damper for seismic control of an integral bridge, in: Structures, 58, Elsevier, 2023, p. 105200.
[35] L.L. Chung, L.Y. Wu, K.H. Lien, H.H. Chen, H.H. Huang, Optimal design of friction pendulum tuned mass damper with varying friction coefficient, Struct. Contr. Health Monit. 20 (4) (2013) 544–559.
[36] S. Chowdhury, S. Adhikari, Nonlinear inertial amplifier liquid column dampers, Appl. Math. Model. 140 (2024) 115875.
[37] S. Chowdhury, A. Jacques, S. Adhikari, Advancing seismic isolation efficiency of rolling rod base isolators using nonlinear inertial amplifiers, Nonlinear Dyn. 113 (2025) 34563–34595.
[38] J.B. Roberts, P.D. Spanos, Random Vibration and Statistical Linearization, Courier Corporation, 2003.
[39] S. Chowdhury, S. Adhikari, Advanced stiffened amplifier friction sliding isolators, J. Struct. Des. Constr. Pract. 31 (3) (2026) 04026049.
[40] J. Den Hartog, J. fourth edition Mechanical, Vibrations, McGraw-Hill Book Company, Inc., New York, 1956.
[41] S. Chowdhury, A. Banerjee, S. Adhikari, From impact to control: inertially amplified friction bearings, ASCE-ASME J. Risk Uncertain. Eng. Syst. A: Civ. Eng. 10 (4) (2024) 04024071.
[42] F. Zamani, S.H. Alavi, M. Mashayekhi, E. Noroozinejad Farsangi, A. Sadeghi-Movahhed, A. Majdi, Optimum design of double tuned mass dampers using multiple metaheuristic multi-objective optimization algorithms under seismic excitation, Front. Built Environ. 11 (2025) 1559530.
[43] M. Abdeddaim, S. Djerouni, M. Basili, Assessment and performance of tuned mass damper inerter design based on genetic algorithm approach for nonlinear structures subjected to earthquake excitation, J. Vib. Eng. Technol. 13 (5) (2025) 353.
[44] A. Pandit, R. Ghiasi, A. Malekjafarian, On the optimization of tuned mass damper inerter (TMDI) systems for buildings subjected to real ground motions using slime mould algorithm, Soil Dyn. Earthq. Eng. 179 (2024) 108557.
[45] H. Garrido, M. Domizio, O. Curadelli, D. Ambrosini, Inerter-based building mass damper: optimization and experimental study, Eng. Struct. 301 (2024) 117277.
[46] J. Song, K. Bi, R. Ma, Z. Wang, K. Xu, H. Hao, Vibration control of adjacent structures equipped with inerter-based dampers considering nonlinearities: analytical and experimental studies, Mech. Syst. Signal Process. 206 (2024) 110903.
[47] M.F. Younes, Optimal design and performance evaluation of dual-configuration inertial amplification tuned mass dampers for enhanced vibration control, J. Eng. Appl. Sci. 72 (1) (2025) 192.
[48] A.E. Abouelregal, M. Marin, A. Öchsner, The influence of a non-local Moore–Gibson–Thompson heat transfer model on an underlying thermoelastic material under the model of memory-dependent derivatives, Contin. Mech. Thermodyn. 35 (2) (2023) 545–562.
[49] S. Sadighi, M. Marin, S. Vlase, Heat transfer analysis of MHD quiescent couple-stress non-Newtonian flow in a porous medium over a stretching/shrinking sheet under PST and PHF conditions: a numerical approach, J. Appl. Math. Mech. Eng. 1 (1) (2026) 2.
[50] M.I. Marin, R.P. Agarwal, I.A. Abbas, Effect of intrinsic rotations, microstructural expansion and contractions in initial boundary value problem of thermoelastic bodies, Bound. Value Probl. 2014 (1) (2014) 129.
[51] A.E. Abouelregal, S.S. Alsaeed, E. Uzun Yaylacı, M. Yaylacı, Fractional DPL thermoelasticity with Rabotnov kernel in a rotating stressed medium with spherical cavity, Math. Methods Appl. Sci. 48 (18) (2025) 16375–16390.
[52] G.B. Warburton, Optimum absorber parameters for various combinations of response and excitation parameters, Earthq. Eng. Struct. Dyn. 10 (3) (1982) 381–401.
[53] M. Zilletti, S.J. Elliott, E. Rustighi, Optimisation of dynamic vibration absorbers to minimise kinetic energy and maximise internal power dissipation, J. Sound Vib. 331 (18) (2012) 4093–4100.
[54] Y. Iwata, On the construction of the dynamic vibration absorbers, Jpn. Soc. Mech. Eng. 820 (8) (1982) 150–152.
[55] Z. Gewei, B. Basu, A study on friction-tuned mass damper: harmonic solution and statistical linearization, J. Vib. Contr. 17 (5) (2011) 721–731.